ACS NANO

www.acsnano.org

ARTICLE

Uncovering the Effects of Metal Contacts on Monolayer MoS_2

Kirstin Schauble, Dante Zakhidov, Eilam Yalon, Sanchit Deshmukh, Ryan W. Grady, Kayla A. Cooley, Connor J. McClellan, Sam Vaziri, Donata Passarello, Suzanne E. Mohney, Michael F. Toney, A. K. Sood, Alberto Salleo, and Eric Pop*

Cite This: ACS Nano 2020, 14, 14798−14808 Read Online

ACCESS | Metrics & More | Article Recommendations | Supporting Information

ABSTRACT: **Metal contacts are a key limiter to the electronic performance of two-dimensional (2D) semiconductor devices. Here, we present a comprehensive study of contact interfaces between seven metals (Y, Sc, Ag, Al, Ti, Au, Ni, with work functions from 3.1 to 5.2 eV) and monolayer MoS_2 grown by chemical vapor deposition. We evaporate thin metal films onto MoS_2 and study the interfaces by Raman spectroscopy, X-ray photoelectron spectroscopy, X-ray diffraction, transmission electron microscopy, and electrical characterization. We uncover that (1) ultrathin oxidized Al dopes MoS_2 *n*-type (>2 × 10^{12} cm^{-2}) without degrading its mobility, (2) Ag, Au, and Ni deposition causes varying levels of damage to MoS_2 (e.g. broadening Raman E′ peak from <3 to >6 cm^{-1}), and (3) Ti, Sc, and Y react with MoS_2. Reactive metals must be avoided in contacts to monolayer MoS_2, but control studies reveal the reaction is mostly limited to the top layer of multilayer films. Finally, we find that (4) thin metals do not significantly strain MoS_2, as confirmed by X-ray diffraction. These are important findings for metal contacts to MoS_2 and broadly applicable to many other 2D semiconductors.**

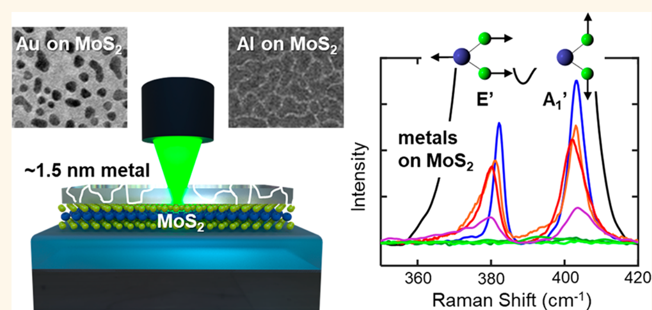

KEYWORDS: *MoS_2, 2D materials, metal contacts, Raman, XPS, doping, strain*

As nanoscale electronic devices decrease in size or as new materials are introduced, the role of their metal contacts becomes increasingly important. For example, contacts to transistors based on organic semiconductors, which are hindered by metal reactivity and poor band alignment,[1,2] are the largest hurdle for realizing high-frequency operation.[3] Even traditional semiconductors like silicon and germanium suffer from Fermi level pinning at the contacts, which frequently creates an unwanted energy barrier for carrier injection, leading to parasitic contact resistance.[4,5] As device dimensions and contact areas continue to shrink, these parasitic resistances increasingly limit transistor performance by dominating the total device resistance.[6]

Among new materials, two-dimensional (2D) semiconductors, such as MoS_2, show promise toward extreme miniaturization of electronics due to superior electrical properties in atomically thin channels compared to silicon-on-insulator (SOI).[7] However, 2D devices also suffer from Fermi level pinning at the metal interface, potentially causing large Schottky barriers (and contact resistance) both for electron and hole injection.[8,9] Efforts have been made to depin the Fermi level and tune the Schottky barrier height of contacts to 2D materials by stamp-transferring metal contacts[10] and by transferring hexagonal boron nitride (*h*-BN) as an interlayer,[11] but these approaches are not industrially scalable and have not yet demonstrated improved contact resistance because they introduce an additional van der Waals tunneling resistance. The lowest contact resistance to undoped *monolayer* MoS_2 (∼1 kΩ·μm) is currently achieved using electron beam (e-beam) evaporated Au or Ag.[12−14] However, further reduction of contact resistance by an order of magnitude is necessary for sub-10-nm scale transistors.[7]

Improving contact resistance to 2D materials requires better understanding of the metal-2D interface, which remains limited in its scope today. Previous studies used X-ray photoelectron spectroscopy (XPS)[15−18] and cross-section transmission electron microscopy (TEM)[19,20] to show that reactions between metals and *multilayer* MoS_2 can occur.

Received: April 27, 2020
Accepted: September 9, 2020
Published: September 9, 2020

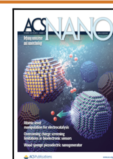

Downloaded via STANFORD UNIV on November 26, 2020 at 01:08:48 (UTC).
See https://pubs.acs.org/sharingguidelines for options on how to legitimately share published articles.

© 2020 American Chemical Society

https://dx.doi.org/10.1021/acsnano.0c03515
ACS Nano 2020, 14, 14798−14808

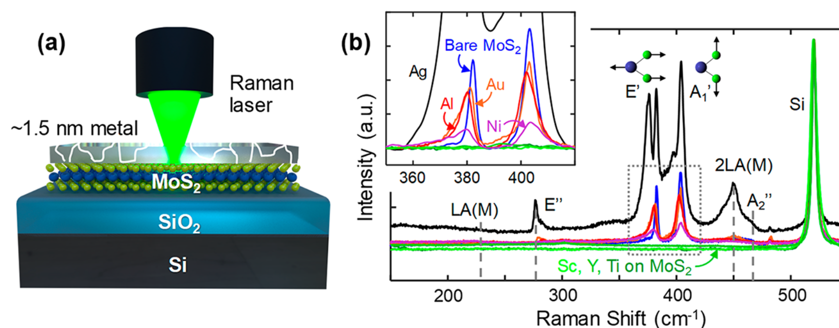

Figure 1. (a) Raman measurement schematic of monolayer MoS_2 coated with ~1.5 nm of evaporated metals. White lines illustrate grain boundaries of the discontinuous metal film (note some metals such as Au and Ag are much more discontinuous). (b) Raman spectra of monolayer MoS_2 bare (blue) and coated with thin metal films (each color represents a different metal, where different shades of green are for the metals which react with MoS_2). All MoS_2 and substrate (Si) peaks are labeled. Atomic cartoons represent in-plane (E′ peak) and out-of-plane (A_1' peak) vibrations of monolayer MoS_2. The inset shows a zoomed in view of the MoS_2 E′ and A_1' peaks (from the boxed region, with baseline subtracted). Changes in MoS_2 peaks indicate modifications of MoS_2 due to metal evaporation. The MoS_2 Raman signal is no longer detectable after deposition of Sc, Y, and Ti due to reactions with MoS_2. Al dopes MoS_2 *n*-type, causing a red-shift of the A_1' peak and an asymmetric Fano shape of the E′ peak. Ag, Au, and Ni damage MoS_2, evidenced by broadening of the E′ peak. Ag enhances the MoS_2 Raman signal due to a surface enhanced Raman scattering (SERS) effect with the 532 nm laser, as reported previously.[25,26] This SERS effect also brings out additional MoS_2 peaks, i.e. the E″ peak at ~287 cm^{-1}, 2LA(M) peak at ~452 cm^{-1}, and A_2'' peak at ~465 cm^{-1}.[31,32] Splitting of the E′ peak for Ag- and Au-covered MoS_2 is due to incomplete coverage of these metals on MoS_2 (see Supporting Information section 1 for peak fitting details).

Table 1. Summary of Work Functions (Φ_M for Polycrystalline Metals[33,34]), Extracted MoS_2 Raman Peak Fitting, and Effects of Metals on MoS_2[a]

	Φ_M (eV)	E′ peak (cm^{-1})	A_1' peak (cm^{-1})	E′ FWHM (cm^{-1})	Strain ε or Δε (XRD)	Doping	Reactions (XPS)
Bare MoS_2	--	382.8	404.0	2.8	ε = 0.4-0.5%	--	--
Ni on MoS_2	5.15	380.4	404.4	6.3	Δε = 0.037%	--	NiO_x
Au on MoS_2	5.1	378.6	403.6	3.6	Δε = 0.012%	--	--
Ti on MoS_2	4.33	--	--	--	Δε = --	--	TiO_x + Ti_xS_y
Al on MoS_2	4.28	380.2	402.9	3.5	Δε = 0.014%	n-type	AlO_x
Ag on MoS_2	4.26	375.1	404.0	3.4	Δε = 0.003%	--	--
Sc on MoS_2	3.5	--	--	--	--	--	ScO_x + Sc_xS_y
Y on MoS_2	3.1	--	--	--	--	--	YO_x + Y_xS_y

[a]Work function of MoS_2 is not listed, as it can vary from ~4 eV (*n*-type, *e.g.*, after AlO_x doping in this work) to ~6 eV (*p*-type), depending on doping. Tensile strain values reported are those measured by grazing incidence XRD. For bare MoS_2, strain (ε) is calculated by comparing the lattice spacing of as-grown MoS_2 with that of transferred MoS_2, where the range is due to variability between growths (see Supporting Information section 6). Strain values for metal-coated MoS_2 are listed as $\Delta\varepsilon$, with respect to the as-grown bare MoS_2. Doping is based on A_1' Raman peak shifting and threshold voltage (V_T) shift in transistor characterization, with Al showing the most evident doping effects. Reaction products listed are based on XPS measurements (see Supporting Information section 2).

However, it is unclear how many layers deep the reactions penetrate the 2D material, which is important for contacts to monolayer *versus* multilayer materials. A previous study points to the lack of interfacial reaction as a requirement for epitaxy of metals on 2D materials,[21] and Ag, Au, Pb, Pd, Pt, Al, Cu, and Zn films were found (by TEM) to grow epitaxially on MoS_2, indicating that these metals do not react with MoS_2.[22] Other studies have reported large strain effects from thin (1−3 nm) evaporated metals on MoS_2 using Raman spectroscopy.[23−26] However, Raman analysis provides only an indirect measurement of strain by assuming shifts in MoS_2 Raman peaks are solely due to strain, so quantification using a direct lattice constant measurement technique, such as X-ray diffraction (XRD), remains necessary.

Here we conduct a comprehensive study of contact interfaces between several metals and monolayer MoS_2 using Raman spectroscopy, XPS, grazing incidence XRD, TEM, and electrical characterization. We deposit thin metal films (Y, Sc, Ag, Al, Ti, Au, and Ni) using high-vacuum e-beam evaporation (~10^{-7} Torr) onto monolayer MoS_2 (additional details in Methods). Raman spectroscopy is used to characterize the metal-coated MoS_2 samples and provide insight on changes in its reactions,[27] carrier concentration,[28] defects,[29] and strain.[30] Compared to other techniques, Raman spectroscopy can be done quickly, nondestructively, and with submicron spatial resolution, which makes it easy to distinguish between MoS_2 monolayers and bilayers, for example. Various techniques are then used to further refine the observations from Raman characterization: (1) XPS reveals details about chemical bonds

https://dx.doi.org/10.1021/acsnano.0c03515
ACS Nano 2020, 14, 14798−14808

and reactions, (2) XRD measures lattice spacings and, therefore, provides direct strain information, and (3) TEM displays the metal morphology on the 2D material. Finally, (4) we build transistor test structures allowing us to correlate the observations from these analytical techniques with changes in electrical transport characteristics (*e.g.*, mobility and doping) of the MoS_2 beneath the metal film.

RESULTS AND DISCUSSION

Figure 1a displays the schematic for the Raman measurement of metal-coated monolayer MoS_2. The MoS_2 was grown by chemical vapor deposition (CVD)[35,36] directly on a 90 nm SiO_2/Si substrate. The nominal deposited metal thickness (~1.5 nm) is transparent to the Raman laser, allowing straightforward measurement of the underlying MoS_2 Raman signatures. Figure 1b shows the Raman spectra of monolayer MoS_2 bare and coated with the ultrathin metal films, where the E' peak corresponds to in-plane and the A_1' peak to out-of-plane atomic vibrations, and intensities are normalized by the Si peak. The inset displays a zoomed in view of changes in the MoS_2 E' and A_1' peaks after metal deposition, which will be discussed in detail throughout this Article. For each metal on MoS_2, three samples were prepared and five spots on each sample were measured, where Figure 1b illustrates representative data and Table 1 shows the average extracted peak information (see Supporting Information section 1 for details on peak fitting).

Interfacial Reactions. We first discuss three of the low work function metals (Y, Sc, and Ti: $\Phi_M \sim 3.1-4.3$ eV), which could be used for *n*-type contacts to 2D semiconductors given the better theoretical alignment of their Fermi level with the 2D material conduction band.[37] Figure 1b reveals that when monolayer MoS_2 is coated with ultrathin films of these metals, the MoS_2 Raman signal is no longer detectable. A broader spectral range (50−1500 cm^{-1}) does not show additional Raman peaks, except those related to the Si substrate (see Supporting Information section 1). This suggests that interfacial reactions between these metals and MoS_2 occur and the resulting compounds do not have Raman-active modes. However, the Raman signal remains present for Y, Sc, and Ti-coated *bilayer* MoS_2 indicating that the reactions mostly affect the top layer of MoS_2 (Figure S1). This is also an important finding, because bilayer and multilayer MoS_2 may have lower Schottky barrier for electron injection than monolayer,[37,38] and thus could benefit from contacts with these reactive metals (provided they do not oxidize), similar to the process of contact silicidation in mainstream silicon technology.[39]

Next, we took XPS data to better understand these interfacial reactions. Figure 2a displays the Mo 3d XPS spectra, showing reaction byproducts of metallic Mo and sulfur-deficient MoS_{2-x} after Ti deposition, confirming that Ti chemically bonds with the sulfur from MoS_2. Figure 2b shows the XPS Ti 2p spectrum, which reveals prominent Ti oxidation and a Ti_xS_y shoulder. Note that there may be additional Ti oxidation states between the TiO_2 and metallic Ti peaks, thus the fits shown here are a simplified approximation. Following a study by Freedy et al.[40] on the oxidation of Ti based on deposition rate and pressure, the Ti in our study (deposited at ~0.5 Å/s and ~10^{-7} Torr) is only partially oxidized (between 25% and 67%) during deposition. This allows the unoxidized Ti to react with MoS_2 during deposition.

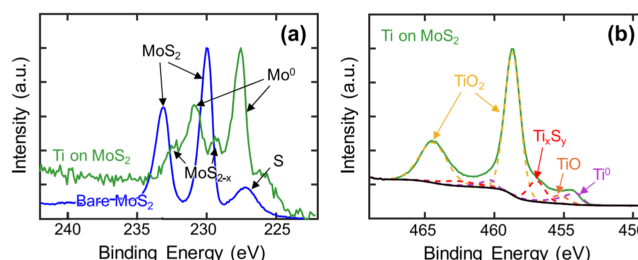

Figure 2. (a) XPS Mo 3d spectrum of MoS_2 bare (blue) and coated with 1.5 nm Ti (green), normalized by their tallest peaks. These spectra reveal evidence of metallic Mo and sulfur-deficient MoS_{2-x} as byproducts of the reaction between Ti and MoS_2. (b) XPS Ti 2p spectrum of Ti-coated MoS_2 (green) and doublet peak fits (dashed lines). Note that Ti_xS_y, TiO, and Ti^0 doublet peaks at higher energy are included in the fit, but the arrows are omitted in this figure. These spectra show evidence of oxidized Ti, Ti_xS_y, and metallic Ti, verifying reaction at Ti-MoS_2 interface. XPS spectra for Sc and Y also show similar signs of oxidation and reaction with MoS_2 (see Figure S3).

Similar oxidation and reactions with MoS_2 occur for Y and Sc, but none of the other metals in this study (Al, Ag, Ni, or Au) show evidence of reactions with MoS_2. XPS data for all samples are shown in Supporting Information section 2, where the ultrathin Al and Ni are found to oxidize after exposure to air, while Au and Ag remain unreactive with MoS_2 and oxygen. However, the Ag-coated MoS_2 sample shows a broadened S 2p spectrum compared to bare MoS_2. Since the Mo 3d spectrum remains unaffected, this suggests that Ag is tarnishing in air (and not reacting with MoS_2). To validate this, we performed selective area electron diffraction (SAED) on the Ag-coated MoS_2 sample, which confirms the presence of MoS_2, polycrystalline Ag, and Ag_2S (see Supporting Information section 3 for SAED data and Methods for SAED sample preparation). Table 1 shows a summary of reactions for each sample studied.

The observed reactions between metals and MoS_2 mostly match expectations based on thermodynamic enthalpies of formation (ΔH) for each metal sulfide and oxide (values reported in Supporting Information section 4). For example, Y, Sc, and Ti sulfides have ΔH (per mole of solid S) that are much more negative than MoS_2, meaning the sulfur atoms in MoS_2 prefer to bond with Y, Sc, and Ti rather than Mo, assuming small entropies of formation and no kinetic limitations. Ag, Au, and Ni have less negative ΔH with sulfur and were not experimentally found to react with MoS_2. Indeed, a previous report has predicted Au to be in thermodynamic equilibrium with MoS_2, while ternary phases in the Ag−Mo−S and Ni−Mo−S systems are reported without corresponding thermodynamic data.[41] The only exception is Al, which has ΔH favoring reaction with sulfur but is not experimentally found to react with MoS_2. This has also been observed in previous studies,[15,17] and can be explained by a larger kinetic barrier for reaction with sulfur, or by Al oxidation since Al_2O_3 also has a very negative ΔH (see Supporting Information section 4).

Doping. Figure 1b reveals red-shifting of the A_1' Raman peak in Al-coated MoS_2, which has been shown to correlate with increased electron concentration ($4.5 \pm 0.5 \times 10^{12}$ electrons/cm^2 per cm^{-1} peak shift).[28,42] Ultrathin Al oxidizes into substoichiometric AlO_x, which is known to behave as an electron charge transfer doping layer for MoS_2[43−45] and

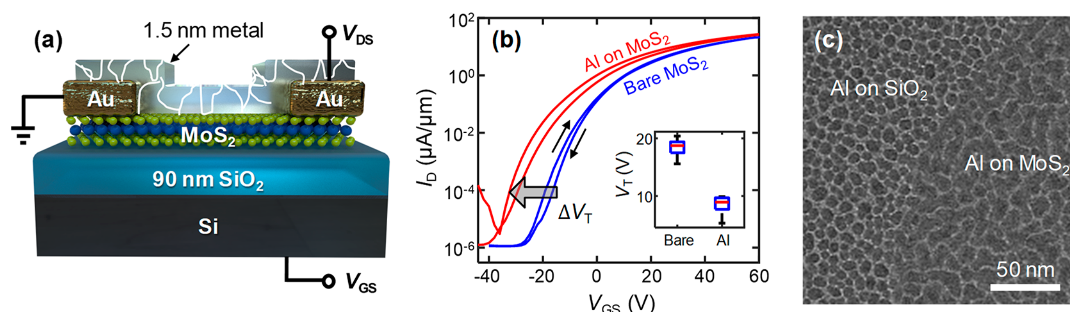

Figure 3. (a) Schematic of back-gated monolayer MoS_2 transistors coated with thin metals (which are neither continuous nor conductive). (b) Device characteristics ($L = 3\ \mu m$, $V_{DS} = 1$ V) before and after capping with 1.5 nm oxidized Al. An average threshold voltage shift $\Delta V_T = -10.1$ V is seen, signifying *n*-type doping of $2.4 \pm 0.5 \times 10^{12}$ electrons/cm^2. Small arrows denote forward and backward voltage sweeps, revealing minimal hysteresis. Inset shows box plot of V_T for bare and Al-coated MoS_2 transistors (10 devices each) with channel lengths of 3−6 μm. (c) Plan view TEM of monolayer CVD MoS_2 covered with ∼1.5 nm Al on an SiO_2 TEM grid, showing Al grains are discontinuous.

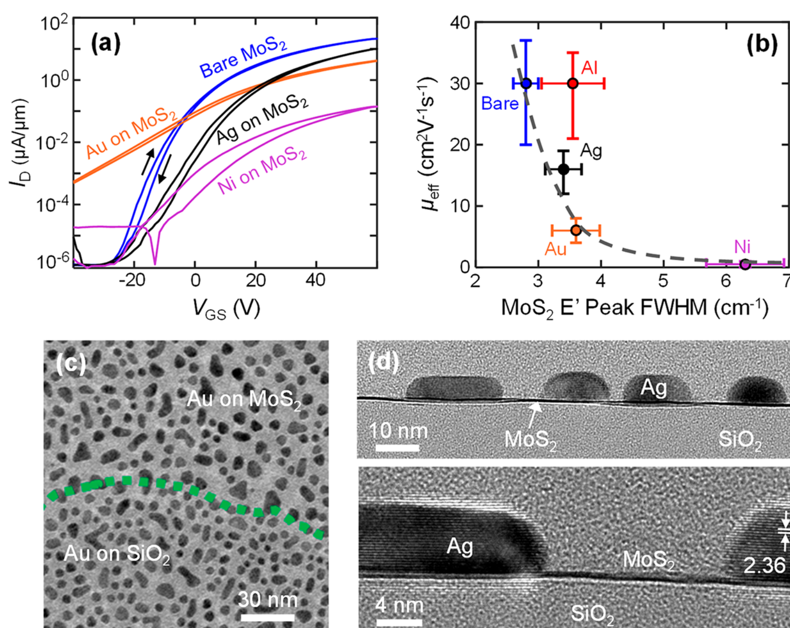

Figure 4. (a) Measured monolayer MoS_2 transistor transfer characteristics ($L = 3\ \mu m$, $V_{DS} = 1$ V) before and after capping with 1.5 nm Ag, Au, and Ni result in degraded I_{on}/I_{off}, mobility, and SS. Small arrows denote forward and backward voltage sweeps. (b) Effective electron mobility (at $n \approx 7 \times 10^{12}$ cm^{-2}) *vs* MoS_2 E′ Raman peak fwhm (gray dashed line to guide the eye). Error bars are from the TLM mobility extraction. (c) Plan view TEM showing discontinuous Au islands on both MoS_2 and SiO_2 (green dashed line shows edge of MoS_2). (d) Top: Cross-section TEM of discontinuous Ag islands on monolayer MoS_2. Bottom: Zoomed in view showing interface between Ag and MoS_2. Ag (111) planes are spaced by 2.36 Å.[61]

$MoSe_2$.[46] Based on the observed A_1' peak shift, the ∼1.5 nm oxidized Al contributes $4.8 \pm 2.7 \times 10^{12}$ electrons/cm^2 doping of MoS_2, where the uncertainty comes from variation in A_1' peak position for bare *versus* Al-coated MoS_2. Electron doping pushes the Fermi level near the conduction band, which can cause optical phonons to interact with the continuum of electronic states. This is evidenced in the MoS_2 Raman spectrum, where an asymmetric Fano line shape can be fit to the Al-coated MoS_2 E′ Raman peak. This Fano line shape has also been reported as evidence of doping for other semiconductors, such as Si, Ge, and carbon nanotubes.[47−50] See Table 1 for positions of the A_1' peak for each metal on MoS_2 and Supporting Information section 1 for further discussion of the Fano fits for each metal on MoS_2.

To verify the doping effect inferred from Raman analysis, we also fabricated MoS_2 transistors, with SiO_2/Si back-gates and Au contacts, then deposited the same ultrathin ∼1.5 nm of metals on the device channels (Figure 3a). The metals are discontinuous, not shorting the source and drain, and preserving an MoS_2 transistor on/off ratio > 10^3 for the nonreactive metals, as shown in Figures 3b and 4a. Our MoS_2 transistors remain strongly *n*-type (even with ultrathin NiO_x islands which could be *p*-type), while control structures using the same ultrathin metals on SiO_2 without the MoS_2 show no measurable conduction. Figures 3c and 4b display plan view TEM images of the thin, discontinuous Al- and Au-coated MoS_2, using the same TEM grids from the SAED analysis. These images further confirm that the MoS_2 device source and drain are not shorted by the thin metal. Figure S5 shows additional plan view TEM images of metal-coated MoS_2 samples, including Ag and Ni.

Figure 3b displays measured drain current *versus* back-gate voltage of the monolayer MoS_2 transistors before and after depositing Al, revealing an average threshold voltage shift ΔV_T

https://dx.doi.org/10.1021/acsnano.0c03515
ACS Nano 2020, 14, 14798−14808

= −10.1 V among 10 devices (see inset of Figure 3b), without degrading mobility or subthreshold swing (SS). This corresponds to n-type doping of 2.4 ± 0.5 × 10^{12} electrons/cm^2 estimated using $\Delta n = |\Delta V_T|C_{ox}/q$, where Δn is the change in electron concentration, $C_{ox} \approx 38$ nF/cm^2 is the oxide capacitance, and q is the elementary charge. This is consistent, within error bars, with the change in carrier concentration estimated independently from Raman analysis, and both support the observation that AlO_x n-type dopes MoS_2. Thus, Al is not a good contact metal (as AlO_x is insulating), but can be used as a damage-free dopant of MoS_2.

Damage. We recall that Figure 1b revealed significant broadening of the MoS_2 E′ Raman peaks after deposition of ultrathin Ni, Au, and Ag. Such broadening is known to occur due to phonon confinement by reduced grain sizes or increased disorder within MoS_2.[32,51−55] Thus, the E′ peak broadening is an indication that the MoS_2 is damaged during the evaporation of these metals, and Table 1 quantifies the full width at half-maximum (fwhm) of this peak for MoS_2 coated with each metal (see Supporting Information section 1 for details on peak fitting). Defects and atomic disorder in multilayer MoS_2 due to Au evaporation has also been reported previously using cross-sectional TEM.[10]

Although we see evidence of disorder in MoS_2 after metal deposition via E′ peak broadening, we do not see the appearance of an LA(M) peak (Figure 1b), which has been shown to appear in very defective MoS_2.[51,53] This places an upper bound on the defect density in our films, <10^{13} cm^{-2} (interdefect distance < 3.2 nm) even after the metal deposition. A lower bound on the defect density of our as-grown films (before metal deposition) is offered by independent transport simulations,[56,57] which found an impurity density of ∼1.5 × 10^{12} cm^{-2} (average separation ∼8 nm) when all impurities are assumed located in the MoS_2 sheet. (We note that photoluminescence can also be used to analyze defects in bare MoS_2 films,[58,59] but metal-induced nonradiative recombination can obscure this effect in our samples.[60])

Figure 4a shows electrical characteristics of monolayer MoS_2 channels covered with ultrathin Ni, Au, and Ag. The transistor on/off ratio degrades from >10^7 for bare MoS_2 to <10^4 for Ni- and Au-coated MoS_2. Figure 4b reveals that the effective mobility (at carrier density $n \approx 7 \times 10^{12}$ cm^{-2}) extracted using transfer length method (TLM) structures,[7,62] also degrades after evaporation of these metals, and scales inversely with MoS_2 E′ peak fwhm. The level of MoS_2 damage (increasing E′ fwhm and decreasing mobility) also scales approximately with metal melting temperature. $Al(O_x)$-covered MoS_2 shows no decrease in mobility, but slight E′ peak broadening is mostly from the asymmetric Fano line shape due to doping. These results indicate that Raman spectroscopy is a useful tool for estimating the electrical quality of a MoS_2 film. See Supporting Information section 5 for additional details on TLM mobility calculations and electrical data of MoS_2 channels covered with the reacting metals (Y, Sc, and Ti).

Figure 4c and 4d shows top-down (plan view) and cross-sectional TEMs of monolayer MoS_2 films (on SiO_2) covered by ultrathin Au and Ag, respectively. Both metals obey Volmer−Weber style island growth on MoS_2,[24] forming only incomplete coverage in such thin films. This is evidence of very weak interaction between Ag and MoS_2, which agrees with the low adhesion energies predicted by density functional theory.[63] Ag islands are face-center cubic (fcc) crystalline and no reactions are observed between Ag and MoS_2, which agrees with our Raman, XPS, and SAED measurements, as well as with previous reports of cross-sectional TEM of Ag on multilayer MoS_2.[22]

There are potential trade-offs of inducing damage to semiconductor contact regions. We have shown that increasing defects in MoS_2 lowers its effective mobility, so the sheet resistance under the contacts will be higher than in the channel.[7,64] However, defects can also improve the contact resistance between the metal and MoS_2, as conductive atomic force microscopy (C-AFM) has shown that charge injection can be higher at MoS_2 defect sites.[65] Other experiments have found up to a 50% decrease in contact resistance when an Ar ion beam was used to induce defects in multilayer MoS_2 before Ni contact deposition.[66] Similarly, etching holes into graphene at the contact regions was found to create improved edge current injection.[67] While the defect density is most likely determined by the metal deposition instrument and parameters, it is interesting to note that some of the best contacts to MoS_2 have been obtained with evaporated Ag,[13,68] Au,[7,12,45] or Ni,[69] suggesting these may be good contacts in part because their deposition creates "just enough" defects in MoS_2, while Au and Ag do not oxidize. In contrast, "defect-free" contacts (*e.g.*, with h-BN depinning layers,[11] transfer-stamped Au,[10] or In deposition[20,70]) suffer from additional van der Waals tunneling resistance. Thus, defect engineering may play an important role in improving contacts to 2D materials.

Strain in As-Grown MoS_2. Strain in 2D materials is often characterized using Raman spectroscopy, by correlating observed peak shifting to strain.[30,71−74] However, many other factors can affect the phonon modes of 2D materials, causing shifts in Raman peaks. Therefore, it is important to confirm Raman-based strain estimates with a direct lattice constant measurement technique. Here, we report a direct measurement of strain in monolayer MoS_2 using grazing incidence XRD at a synchrotron radiation light source. By measuring a large polycrystalline MoS_2 film in grazing incidence with high-energy X-rays, we measure the strain of monolayer MoS_2, which is compared with Raman-based strain analysis.

We first measure the built-in strain of our as-grown monolayer MoS_2. Because of the larger MoS_2 thermal coefficient of expansion compared to SiO_2, the high-temperature (850 °C) CVD growth process results in tensile-strained MoS_2. This causes an E′ Raman peak red-shift, consistent with previous observations.[75] Comparing the E′ Raman peak position of CVD-grown *versus* transferred MoS_2 (where transferring is assumed to relax built-in strain), we estimate that our as-grown MoS_2 is biaxially tensile strained ∼0.4 to 0.5%, depending on the growth. This is based on a calibration of 4.5 cm^{-1} E′ peak shift per percent of biaxial strain, as reported by Li et al.[73] We then used grazing incidence XRD to analyze the monolayer MoS_2 in-plane (10) peak before and after MoS_2 transfer, which verified that the strain values measured from Raman peak shifting were accurate within ∼0.02% strain (Supporting Information section 6). The 0.02% mismatch is within the distribution of strains of CVD-grown MoS_2 calculated using a Williamson−Hall analysis of several monolayer MoS_2 growths (see Supporting Information section 6). These Raman and XRD results also confirm the ∼4.5 cm^{-1} MoS_2 E′ Raman peak red-shift per percent of biaxial tensile strain.[73] Based on these measurements, we find that Raman analysis can be useful to determine built-in strain in *bare* as-

https://dx.doi.org/10.1021/acsnano.0c03515
ACS Nano 2020, 14, 14798−14808

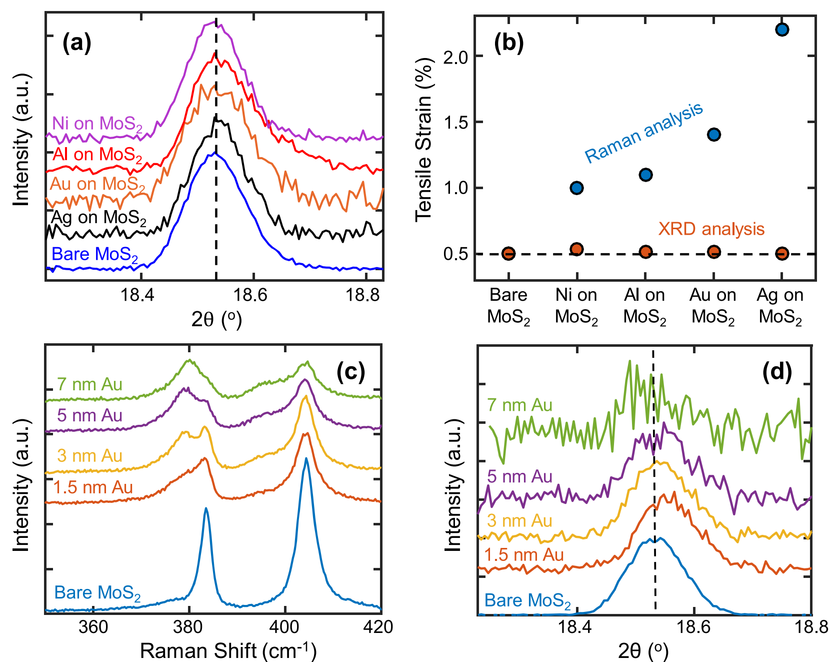

Figure 5. (a) Monolayer MoS_2 XRD in-plane (10) peaks with deposited contact metals show no appreciable strain compared to bare MoS_2. (b) Comparison of MoS_2 strain for each sample as characterized by both Raman and grazing incidence XRD, which reveals that Raman analysis greatly overestimates MoS_2 strain due to thin metals. (c) Raman spectra for MoS_2 bare and coated with 1.5, 3, 5, and 7 nm of deposited Au. This confirms that there are two E' peaks (since thin Au deposits in islands), and the red-shifted peak becomes more prominent as Au coverage on MoS_2 increases. (d) XRD peaks for the same MoS_2 samples coated with thicker Au confirm that even as Au gets thicker (and thus more complete coverage of Au on MoS_2), the measured strain of MoS_2 does not change.

grown 2D materials, which has been previously used for WSe_2.[76] However, we will show in the next section that in more complicated systems, such as MoS_2 coated with metals, Raman analysis of MoS_2 strain is not accurate.

Strain in Metal-Covered MoS_2. As strain can affect the metal-2D semiconductor band alignment,[77] it is important to understand and accurately represent strain in the semiconductor contact regions. The Raman spectra of as-grown MoS_2 after metal deposition (Figure 1b) reveal red-shifting of the E′ peak position, which is typically attributed to strain. The largest E′ peak shift (7.6 cm^{-1}) from the already shifted as-grown bare MoS_2 is seen in the Ag-coated sample, which would suggest that the MoS_2 is biaxially tensile strained by ∼1.7% from the thin metal, in addition to the ∼0.5% built-in MoS_2 strain from CVD growth. Similar claims of MoS_2 strain due to thin (1−3 nm) Au and Ag based on Raman analysis have been previously reported,[23−26] but until now, this remains unconfirmed using a direct strain measurement technique.

Here, we perform grazing incidence XRD to directly measure the CVD-grown monolayer MoS_2 lattice constant with and without thin deposited Ni, Al, Au, and Ag. Testing three samples for each metal, we found that none of the metals appreciably strain the underlying MoS_2. Figure 5a shows one set of samples displaying that the MoS_2 (10) peak does not shift for any deposited thin metal film. Figure 5b shows the average calculated strain (across three samples for each metal) based on Raman and XRD analysis, where XRD reveals <0.04 ± 0.02% average change in strain from the as-grown monolayer MoS_2. This indicates that thin metals do not significantly strain monolayer MoS_2. Cross-section TEM images in Figure 4d show no evidence of MoS_2 strain due to Ag, which would typically manifest as bowing of MoS_2 around the Ag nanoparticles. This supports our conclusion that Ag (the metal which Raman analysis predicts causes the most strain) does not strain MoS_2. Furthermore, the fwhm of the MoS_2 (10) peak (Figure 5a) is consistent across all bare and metal-coated MoS_2 samples (see Supporting Information section 6), which reveals that there is also no change of MoS_2 strain *distribution* due to contact metals.

We recall that most thin metals (especially Au, see Figure 4c) form incomplete coverage on MoS_2. To test if metal continuity affects the strain measurements, we deposit 1.5, 3, 5, and 7 nm of Au on monolayer MoS_2 and compare the Raman and grazing incidence XRD data. In Figure 5c, the Raman spectra of MoS_2 with thicker Au show that the shifted E′ peak (from regions of MoS_2 covered by Au) becomes more dominant with increased Au coverage. However, grazing incidence XRD measurements on the same samples, in Figure 5d, indicate that increasing the metal thickness and coverage still does not strain the underlying MoS_2. Therefore, based on the XRD results presented here, we conclude that using Raman peak shifts alone is likely to lead to an overestimate of strain in MoS_2 under thin metals.

The discrepancy between the Raman and XRD measurements of strain is due to the nature of the experimental techniques. XRD measures the constructive scattering of ordered lattice spacings, which is a direct measurement of the material strain. On the other hand, Raman-based estimates rely on calibrating shifts of phonon modes to strain, assuming that strain is the only factor affecting the phonon modes. However, shifts of the MoS_2 E′ peak can arise from other effects, such as increased disorder (defect density),[51,53−55] or decreased domain size[32,52] of MoS_2. It has also been shown that Au and Ag-coated MoS_2, which exhibit the largest E′ peak shifts, induce plasmon coupling with MoS_2 excitons.[78] This

https://dx.doi.org/10.1021/acsnano.0c03515
ACS Nano 2020, 14, 14798−14808

causes a coupling of phonons to the MoS_2 electronic continuum, which likely contributes to E′ peak red-shifting.

Discussion. While these experiments were performed with monolayer MoS_2, the methodologies and results from this work can be used to draw hypotheses about contacts to other 2D materials. For example, in this study, most contact metal−MoS_2 reactions follow what is expected based on thermodynamics. Therefore, thermodynamic analysis can be carried out for projections of expected metal reactions with selenides and tellurides, and indeed, a recent experimental report of metal epitaxy and reactivity with few-layer WSe_2 was consistent with calculated isothermal phase diagrams.[21] Defect sites may also enhance a 2D material's reactivity,[18,79] which is an important consideration as selenides and tellurides tend to be more defective than sulfides, and CVD-grown 2D materials tend to be more defective than exfoliated 2D materials.[55] Additionally, since the bond energy is weaker for Mo−Te and Mo−Se than Mo−S,[55,80] it is reasonable to expect that they would be even more susceptible to metal evaporation-induced damage and reactions at their contacts.[11] As 2D monolayers represent the ultimate channel thinness limit for all semiconductors, the lessons gleaned here could also benefit other semiconductors in this extreme limit.

Finally, we briefly discuss our vision to improve contact resistance to 2D semiconductors based on the findings in this study and lessons from past generations of contact engineering. First, Schottky barrier widths must be decreased by doping the source and drain regions. Few results, including those shown in this work with AlO_x, have demonstrated such doping through charge transfer from nonstoichiometric oxide capping layers to MoS_2.[44,45,68] Second, reacting the contact metal with the 2D semiconductor may be used to create a more intimate contact interface, as is well-known from silicide contacts for Si devices.[39] This intimate contact interface may also be achieved by defect engineering (tuning defect density in the contact region, *e.g.*, by adjusting deposition techniques and parameters). However, we have shown that defects and reactions can destroy a monolayer 2D material, but do not completely destroy a bilayer material. Therefore, thicker 2D material at the contacts should be explored (*e.g.*, by regrowth), not unlike "raised source/drain" of Si devices,[81] where only the top one or two layers react with the metal and the bottom layers remain unharmed. Third, the contact metal band alignment with the 2D semiconductor may be tuned by Fermi level depinning,[11] or alloying and strain, as was previously achieved by alloying Ge into Si source/drain regions to improve *p*-type contacts.[82] Further efforts in each of these areas are critical to reduce contact resistance below 100 Ω·μm for 2D semiconductors.

CONCLUSIONS

In summary, we deposited thin films of Y, Sc, Ag, Al, Ti, Au, and Ni on monolayer MoS_2 and studied the contact interface by Raman spectroscopy, XPS, XRD, TEM, and electrical characterization. We found through Raman spectroscopy and XPS that low work function metals (Y, Sc, and Ti, often used as adhesion layers) oxidize and react with the underlying monolayer MoS_2, which negatively impacts the contact resistance. We also showed through Raman spectroscopy and electrical characterization that ultrathin Al oxidizes and dopes MoS_2, while Ag, Au, and Ni show varying levels of damage to MoS_2. Lastly, we analyzed the strain effects of metals on MoS_2 using Raman spectroscopy and XRD, noting discrepancies between the two techniques, and we conclude that the thin evaporated metals studied do not strain MoS_2, contrary to previous reports. The findings in this work, as well as the implications discussed for other 2D materials, are crucial for understanding and improving metal contacts to 2D semiconductor devices.

METHODS

Sample Preparation. Monolayer MoS_2 (in the 2H semiconducting phase) is grown directly onto 90 nm SiO_2/Si substrates by CVD using solid sulfur and MoO_3 precursors, and perylene-3,4,9,10 tetracarboxylic acid tetrapotassium salt (PTAS) as a seeding layer. MoS_2 growths take place at 760 Torr and 850 °C, with an Ar flow rate of 30 sccm. The growth results in large (∼30−80 μm) MoS_2 triangles near the edges of the chip which converge into a continuous film in the center of the chip. The MoS_2 is a primarily monolayer film with sparse (<10%) regions of bilayer MoS_2.[35] Additional details on the MoS_2 growth can be found in Smithe et al.[35,36] Thin metals (∼1.5 nm, measured by crystal monitor) were deposited using the Kurt. J. Lesker PVD 75 e-beam evaporation system in high vacuum (∼10^{-7} Torr) at a rate of ∼0.5 Å/s. Each metal was deposited on 3 separate MoS_2 growths to ensure repeatability of results.

Raman Measurements. All Raman measurements were taken using the Horiba Labram HR Evolution Raman System in the Stanford Nanofabrication Shared Facility. A green laser source of wavelength 532 nm was used with 2.5% incident laser power (0.12 mW) to avoid heating effects, and the spot size is less than 1 μm. An 1800 grooves/mm grating was used, resulting in a spectral resolution of ∼0.3 cm^{-1}. Peak fitting details are described in Supporting Information section 1.

XPS Measurements. All XPS measurements were taken in the Stanford Nanofabrication Shared Facility using a PHI VersaProbe III scanning XPS microprobe. The XPS instrument uses a monochromatized Al(Ka) radiation (1486 eV) as source of incident X-rays. We performed all measurements at a chamber pressure <10^{-6} Torr. The X-ray spot size was ∼100 μm with 100 W incident power (high power). Additionally, we performed auto sample neutralization to overcome sample charging effects. The XPS analysis and peak fitting was performed in CasaXPS.

Plan View TEM Measurements. MoS_2 was grown onto SPI 20 nm SiO_2 TEM grids, and subsequent metal evaporation was performed as described above. The MoS_2 growth process was the same as described in the Sample Preparation section, however, instead of using the PTAS seeding layer directly on the growth substrate, a separate chip covered in PTAS was placed directly upstream from the growth substrate. This different growth geometry was due to the small size of the TEM grid substrates. Plan view TEM and SAED examination were performed using a FEI Talos F200X in the Materials Characterization Laboratory at The Pennsylvania State University. All samples were analyzed using an accelerating voltage of 80 kV to limit e-beam damage of the MoS_2. The imaging data provided insight concerning the size of metal nuclei on the MoS_2 surface as well as their continuity. Electron diffraction patterns provided information concerning whether the metal nuclei were epitaxial or randomly oriented on the MoS_2 surface.

XRD Measurements. All XRD measurements were taken at the Stanford Synchrotron Radiation Lightsource beamline 7−2, where the diffraction geometry is illustrated in Figure S11. The polycrystalline nature of the CVD-grown MoS_2 samples enabled the diffraction conditions necessary to obtain MoS_2 signal. The sample was attached to a six-circle diffractometer with the sample plane vertical during the measurements. The sample was covered with a Kapton dome and purged with helium gas to improve signal-to-noise ratio by reducing air scattering. The 14 keV (0.885 Å) incident beam was set to grazing incidence (0.1°) relative to the sample surface and the scattered radiation was collimated to 1 mrad by Soller slits and collected by a Vortex point detector. The sample was rocked during the measurement to remove potential beam damage, and each measurement was averaged over 3 exposures to further reduce noise. Based on the grazing incidence angle and sample rocking, the effective sample

https://dx.doi.org/10.1021/acsnano.0c03515
ACS Nano 2020, 14, 14798−14808

measurement area is ~2.8 mm wide by the whole length of the sample (~7−12 mm). Therefore, like the XPS measurements, sparse (<10%) bilayer MoS_2 regions are included in the XRD signal. The experimental setup was calibrated using a lanthanum hexaboride standard.

Device Fabrication and Measurement. All device fabrication was performed in the Stanford Nanofabrication Facility. Optical lithography is used to define probe pads, electrical contacts, and channels in three separate steps. O_2 plasma (10 W) is used to etch the MoS_2 for channel definition.[36] Au is evaporated using e-beam evaporation as a planar contact to the MoS_2. Finally, the substrate is loaded into a Janis vacuum probe station (~10^{-5} Torr) for measurements using a Keithley 4200-SCS. After measurements, devices were coated with a thin layer (~1.5 nm) of metals using the e-beam evaporation parameters outlined above, then remeasured using the same Janis setup. At least 10 transistors were measured for each sample, before and after coating with metal, to ensure consistency of results.

ASSOCIATED CONTENT

Supporting Information

The Supporting Information is available free of charge at https://pubs.acs.org/doi/10.1021/acsnano.0c03515.

> Additional details on Raman measurements and analysis, XPS measurements, SAED measurements, thermodynamic analysis, Fano line fits, plan view TEM measurements, TLM mobility extraction, electrical characterization of low work function metals on MoS_2, strain measurements of as-grown monolayer MoS_2, and X-ray diffraction measurements (PDF)

AUTHOR INFORMATION

Corresponding Author

Eric Pop − *Department of Electrical Engineering, Department of Materials Science and Engineering, and Precourt Institute for Energy, Stanford University, Stanford, California 94305, United States;* orcid.org/0000-0003-0436-8534; Email: epop@stanford.edu

Authors

Kirstin Schauble − *Department of Electrical Engineering, Stanford University, Stanford, California 94305, United States;* orcid.org/0000-0002-4130-9181

Dante Zakhidov − *Department of Materials Science and Engineering, Stanford University, Stanford, California 94305, United States;* orcid.org/0000-0003-3107-104X

Eilam Yalon − *Department of Electrical Engineering, Stanford University, Stanford, California 94305, United States;* orcid.org/0000-0001-7965-459X

Sanchit Deshmukh − *Department of Electrical Engineering, Stanford University, Stanford, California 94305, United States;* orcid.org/0000-0003-1848-2127

Ryan W. Grady − *Department of Electrical Engineering, Stanford University, Stanford, California 94305, United States;* orcid.org/0000-0002-0457-5026

Kayla A. Cooley − *Department of Materials Science and Engineering, The Pennsylvania State University, University Park, Pennsylvania 16802, United States;* orcid.org/0000-0002-6598-4296

Connor J. McClellan − *Department of Electrical Engineering, Stanford University, Stanford, California 94305, United States;* orcid.org/0000-0002-8733-9968

Sam Vaziri − *Department of Electrical Engineering, Stanford University, Stanford, California 94305, United States;* orcid.org/0000-0003-1234-6060

Donata Passarello − *Stanford Synchrotron Radiation Lightsource, SLAC National Accelerator Laboratory, Menlo Park, California 94025, United States*

Suzanne E. Mohney − *Department of Materials Science and Engineering, The Pennsylvania State University, University Park, Pennsylvania 16802, United States*

Michael F. Toney − *Stanford Synchrotron Radiation Lightsource, SLAC National Accelerator Laboratory, Menlo Park, California 94025, United States;* orcid.org/0000-0002-7513-1166

A. K. Sood − *Department of Physics, India Institute of Science, Bangalore 560012, India;* orcid.org/0000-0002-4157-361X

Alberto Salleo − *Department of Materials Science and Engineering, Stanford University, Stanford, California 94305, United States*

Complete contact information is available at: https://pubs.acs.org/10.1021/acsnano.0c03515

Notes

The authors declare no competing financial interest.
A preprint of this manuscript was published on arXiv.[83]

ACKNOWLEDGMENTS

This work was supported in part by ASCENT, one of six centers in JUMP, a Semiconductor Research Corporation (SRC) program sponsored by DARPA. It is also supported by the National Science Foundation (NSF) EFRI 2-DARE, the Air Force Grant FA9550-14-1-0251, and the Stanford SystemX Alliance. Work was performed in part at the Stanford Nanofabrication Facility and the Stanford Nano Shared Facilities, which are supported by the NSF as part of the National Nanotechnology Coordinated Infrastructure under Award ECCS-1542152. Use of the Stanford Synchrotron Radiation Lightsource at SLAC National Accelerator Laboratory was supported by the U.S. Department of Energy, Office of Basic Energy Sciences under Contract DE-AC02-76SF00515. Plan view TEM was supported by NSF through DMR 1410334. We thank Adedapo Oni for cross section TEM measurements and support and Intel Corporation for funding. K.S. thanks the NSF Graduate Research Fellowship Program (GRFP), under Grant DGE-1656518, and the Stanford Graduate Fellowships for support. D.Z. and R.W.G. also acknowledge support by the NSF GRFP under Grant DGE-1656518, and K.A.C. thanks the NSF GRFP Grant No. DGE-1255832 for support. The Knut and Alice Wallenberg Foundation partially supported S.V. through a postdoctoral fellowship. A.K.S. thanks Department of Science and Technology, India, for Year of Science Professorship which funded the travel to facilitate the collaboration.

REFERENCES

(1) de Boer, B.; Hadipour, A.; Mandoc, M. M.; van Woudenbergh, T.; Blom, P. W. M. Tuning of Metal Work Functions with Self-Assembled Monolayers. *Adv. Mater.* **2005**, *17*, 621−625.

(2) Lamport, Z. A.; Barth, K. J.; Lee, H.; Gann, E.; Engmann, S.; Chen, H.; Guthold, M.; McCulloch, I.; Anthony, J. E.; Richter, L. J.; DeLongchamp, D. M.; Jurchescu, O. D. A Simple and Robust Approach to Reducing Contact Resistance in Organic Transistors. *Nat. Commun.* **2018**, *9*, 5130.

(3) Klauk, H. Will We See Gigahertz Organic Transistors? *Adv. Electron. Mater.* **2018**, *4*, 1700474.
(4) Dimoulas, A.; Tsipas, P.; Sotiropoulos, A.; Evangelou, E. K. Fermi-Level Pinning and Charge Neutrality Level in Germanium. *Appl. Phys. Lett.* **2006**, *89*, 252110.
(5) Himpsel, F. J.; Hollinger, G.; Pollak, R. A. Determination of the Fermi-Level Pinning Position at Si(111) Surfaces. *Phys. Rev. B: Condens. Matter Mater. Phys.* **1983**, *28*, 7014−7018.
(6) Thompson, S. E.; Parthasarathy, S. Moore's Law: The Future of Si Microelectronics. *Mater. Today* **2006**, *9*, 20−25.
(7) English, C. D.; Shine, G.; Dorgan, V. E.; Saraswat, K. C.; Pop, E. Improved Contacts to MoS_2 Transistors by Ultra-High Vacuum Metal Deposition. *Nano Lett.* **2016**, *16*, 3824−3830.
(8) Gong, C.; Colombo, L.; Wallace, R. M.; Cho, K. The Unusual Mechanism of Partial Fermi Level Pinning at Metal-MoS_2 Interfaces. *Nano Lett.* **2014**, *14*, 1714−1720.
(9) Allain, A.; Kang, J.; Banerjee, K.; Kis, A. Electrical Contacts to Two-Dimensional Semiconductors. *Nat. Mater.* **2015**, *14*, 1195−1205.
(10) Liu, Y.; Guo, J.; Zhu, E. B.; Liao, L.; Lee, S. J.; Ding, M. N.; Shakir, I.; Gambin, V.; Huang, Y.; Duan, X. F. Approaching the Schottky-Mott Limit in van der Waals Metal-Semiconductor Junctions. *Nature* **2018**, *557*, 696−700.
(11) Mleczko, M. J.; Yu, A. C.; Smyth, C. M.; Chen, V.; Shin, Y. C.; Chatterjee, S.; Tsai, Y. C.; Nishi, Y.; Wallace, R. M.; Pop, E. Contact Engineering High-Performance *n*-Type $MoTe_2$ Transistors. *Nano Lett.* **2019**, *19*, 6352−6362.
(12) English, C. D.; Smithe, K. K. H.; Xu, R. J.; Pop, E. Approaching Ballistic Transport in Monolayer MoS_2 Transistors with Self-Aligned 10 nm Top Gates. *IEEE Int. Electron Devices Meet.* **2016**, 5.6.1−5.6.4.
(13) Smithe, K. K. H.; English, C. D.; Suryavanshi, S. V.; Pop, E. High-Field Transport and Velocity Saturation in Synthetic Monolayer MoS_2. *Nano Lett.* **2018**, *18*, 4516−4522.
(14) McClellan, C.; Suryavanshi, S.; English, C.; Smithe, K.; Bailey, C.; Grady, R.; Pop, E. *2D Semiconductor Transistor Device Trends*. http://2d.stanford.edu/2D_Trends (accessed April 1, 2020).
(15) Lince, J. R.; Carre, D. J.; Fleischauer, P. D. Schottky-Barrier Formation on a Covalent Semiconductor without Fermi-Level Pinning: The Metal-MoS_2(0001) Interface. *Phys. Rev. B: Condens. Matter Mater. Phys.* **1987**, *36*, 1647−1656.
(16) McDonnell, S.; Smyth, C.; Hinkle, C. L.; Wallace, R. M. MoS_2-Titanium Contact Interface Reactions. *ACS Appl. Mater. Interfaces* **2016**, *8*, 8289−8294.
(17) McGovern, I. T.; Dietz, E.; Rotermund, H. H.; Bradshaw, A. M.; Braun, W.; Radlik, W.; Mcgilp, J. F. Soft-X-Ray Photoemission Spectroscopy of Metal Molybdenum-Disulfide Interfaces. *Surf. Sci.* **1985**, *152*, 1203−1212.
(18) Smyth, C. M.; Addou, R.; McDonnell, S.; Hinkle, C. L.; Wallace, R. M. Contact Metal-MoS_2 Interfacial Reactions and Potential Implications on MoS_2-Based Device Performance. *J. Phys. Chem. C* **2016**, *120*, 14719−14729.
(19) Kim, C.; Moon, I.; Lee, D.; Choi, M. S.; Ahmed, F.; Nam, S.; Cho, Y.; Shin, H. J.; Park, S.; Yoo, W. J. Fermi Level Pinning at Electrical Metal Contacts of Monolayer Molybdenum Dichalcogenides. *ACS Nano* **2017**, *11*, 1588−1596.
(20) Wu, R. J.; Udyavara, S.; Ma, R.; Wang, Y.; Chhowalla, M.; Birol, T.; Koester, S. J.; Neurock, M.; Mkhoyan, K. A. Visualizing the Metal-MoS_2 Contacts in Two-Dimensional Field-Effect Transistors with Atomic Resolution. *Phys. Rev. Mater.* **2019**, *3*, 111001.
(21) Cooley, K. A.; Alsaadi, R.; Gurunathan, R. L.; Domask, A. C.; Kerstetter, L.; Saidi, W. A.; Mohney, S. E. Room-Temperature Epitaxy of Metal Thin Films on Tungsten Diselenide. *J. Cryst. Growth* **2019**, *505*, 44−51.
(22) Domask, A. C.; Cooley, K. A.; Kabius, B.; Abraham, M.; Mohney, S. E. Room Temperature van der Waals Epitaxy of Metal Thin Films on Molybdenum Disulfide. *Cryst. Growth Des.* **2018**, *18*, 3494−3501.
(23) Golasa, K.; Grzeszczyk, M.; Binder, J.; Bozek, R.; Wysmolek, A.; Babinski, A. The Disorder-Induced Raman Scattering in Au/MoS_2 Heterostructures. *AIP Adv.* **2015**, *5*, 077120.
(24) Gong, C.; Huang, C. M.; Miller, J.; Cheng, L. X.; Hao, Y. F.; Cobden, D.; Kim, J.; Ruoff, R. S.; Wallace, R. M.; Cho, K.; Xu, X. D.; Chabal, Y. J. Metal Contacts on Physical Vapor Deposited Monolayer MoS_2. *ACS Nano* **2013**, *7*, 11350−11357.
(25) Moe, Y. A.; Sun, Y. H.; Ye, H. Y.; Liu, K.; Wang, R. M. Probing Evolution of Local Strain at MoS_2-Metal Boundaries by Surface-Enhanced Raman Scattering. *ACS Appl. Mater. Interfaces* **2018**, *10*, 40246−40254.
(26) Sun, Y. H.; Liu, K.; Hong, X. P.; Chen, M.; Kim, J.; Shi, S. F.; Wu, J. Q.; Zettl, A.; Wang, F. Probing Local Strain at MX_2-Metal Boundaries with Surface Plasmon-Enhanced Raman Scattering. *Nano Lett.* **2014**, *14*, 5329−5334.
(27) Agyapong, A. D.; Cooley, K. A.; Mohney, S. E. Reactivity of Contact Metals on Monolayer WS_2. *J. Appl. Phys.* **2020**, *128*, 055306.
(28) Chakraborty, B.; Bera, A.; Muthu, D. V. S.; Bhowmick, S.; Waghmare, U. V.; Sood, A. K. Symmetry-Dependent Phonon Renormalization in Monolayer MoS_2 Transistor. *Phys. Rev. B: Condens. Matter Mater. Phys.* **2012**, *85*, 161403.
(29) Carvalho, B. R.; Wang, Y. X.; Mignuzzi, S.; Roy, D.; Terrones, M.; Fantini, C.; Crespi, V. H.; Malard, L. M.; Pimenta, M. A. Intervalley Scattering by Acoustic Phonons in Two-Dimensional MoS_2 Revealed by Double-Resonance Raman Spectroscopy. *Nat. Commun.* **2017**, *8*, 14670.
(30) Rice, C.; Young, R. J.; Zan, R.; Bangert, U.; Wolverson, D.; Georgiou, T.; Jalil, R.; Novoselov, K. S. Raman-Scattering Measurements and First-Principles Calculations of Strain-Induced Phonon Shifts in Monolayer MoS_2. *Phys. Rev. B: Condens. Matter Mater. Phys.* **2013**, *87*, 081307.
(31) Ataca, C.; Topsakal, M.; Aktürk, E.; Ciraci, S. A Comparative Study of Lattice Dynamics of Three- and Two-Dimensional MoS_2. *J. Phys. Chem. C* **2011**, *115*, 16354−16361.
(32) Frey, G. L.; Tenne, R.; Matthews, M. J.; Dresselhaus, M. S.; Dresselhaus, G. Raman and Resonance Raman Investigation of MoS_2 Nanoparticles. *Phys. Rev. B: Condens. Matter Mater. Phys.* **1999**, *60*, 2883−2892.
(33) Michaelson, H. B. Work Function of Elements and Its Periodicity. *J. Appl. Phys.* **1977**, *48*, 4729−4733.
(34) Uda, M.; Nakamura, A.; Yamamoto, T.; Fujimoto, Y. Work Function of Polycrystalline Ag, Au and Al. *J. Electron Spectrosc. Relat. Phenom.* **1998**, *88*, 643−648.
(35) Smithe, K. K. H.; English, C. D.; Suryavanshi, S. V.; Pop, E. Intrinsic Electrical Transport and Performance Projections of Synthetic Monolayer MoS_2 Devices. *2D Mater.* **2017**, *4*, 011009.
(36) Smithe, K. K. H.; Suryavanshi, S. V.; Muñoz Rojo, M.; Tedjarati, A. D.; Pop, E. Low Variability in Synthetic Monolayer MoS_2 Devices. *ACS Nano* **2017**, *11*, 8456−8463.
(37) Zhong, H.; Quhe, R.; Wang, Y.; Ni, Z.; Ye, M.; Song, Z.; Pan, Y.; Yang, J.; Yang, L.; Lei, M.; et al. Interfacial Properties of Monolayer and Bilayer MoS_2 Contacts with Metals: Beyond the Energy Band Calculations. *Sci. Rep.* **2016**, *6*, 21786.
(38) Lee, H.; Deshmukh, S.; Wen, J.; Costa, V. Z.; Schuder, J. S.; Sanchez, M.; Ichimura, A. S.; Pop, E.; Wang, B.; Newaz, A. K. M. Layer-Dependent Interfacial Transport and Optoelectrical Properties of MoS_2 on Ultraflat Metals. *ACS Appl. Mater. Interfaces* **2019**, *11*, 31543−31550.
(39) Ohguro, T.; Nakamura, S.; Saito, M.; Ono, M.; Harakawa, H.; Morifuji, E.; Yoshitomi, T.; Morimoto, T.; Momose, H. S.; Katsumata, Y.; Iwai, H. Ultra-Shallow Junction and Salicide Techniques for Advanced CMOS Devices. *ULSI Sci. Technol. Conf.* **1997**, 275−295.
(40) Freedy, K. M.; Giri, A.; Foley, B. M.; Barone, M. R.; Hopkins, P. E.; McDonnell, S. Titanium Contacts to Graphene: Process-Induced Variability in Electronic and Thermal Transport. *Nanotechnology* **2018**, *29*, 145201.
(41) Domask, A. C.; Gurunathan, R. L.; Mohney, S. E. Transition Metal-MoS_2 Reactions: Review and Thermodynamic Predictions. *J. Electron. Mater.* **2015**, *44*, 4065−4079.

(42) Michail, A.; Delikoukos, N.; Parthenios, J.; Galiotis, C.; Papagelis, K. Optical Detection of Strain and Doping Inhomogeneities in Single Layer MoS_2. *Appl. Phys. Lett.* **2016**, *108*, 173102.
(43) Kim, S. Y.; Yang, H. I.; Choi, W. Photoluminescence Quenching in Monolayer Transition Metal Dichalcogenides by Al_2O_3 Encapsulation. *Appl. Phys. Lett.* **2018**, *113*, 133104.
(44) Leonhardt, A.; Chiappe, D.; Afanas'ev, V. V.; El Kazzi, S.; Shlyakhov, I.; Conard, T.; Franquet, A.; Huyghebaert, C.; de Gendt, S. Material-Selective Doping of 2D TMDC through Al_xO_y Encapsulation. *ACS Appl. Mater. Interfaces* **2019**, *11*, 42697−42707.
(45) McClellan, C. J.; Yalon, E.; Smithe, K. K. H.; Suryavanshi, S. V.; Pop, E. Effective *n*-type Doping of Monolayer MoS_2 by AlO_x. *IEEE Device Res. Conf.* **2017**, 1−2.
(46) Somvanshi, D.; Ber, E.; Bailey, C. S.; Pop, E.; Yalon, E. Improved Current Density and Contact Resistance in Bilayer $MoSe_2$ Field Effect Transistors by AlO_x Capping. *ACS Appl. Mater. Interfaces* **2020**, *12*, 36355−36361.
(47) Nickel, N. H.; Lengsfeld, P.; Sieber, I. Raman Spectroscopy of Heavily Doped Polycrystalline Silicon Thin Films. *Phys. Rev. B: Condens. Matter Mater. Phys.* **2000**, *61*, 15558−15561.
(48) Cerdeira, F.; Fjeldly, T. A.; Cardona, M. Effect of Free Carriers on Zone-Center Vibrational Modes in Heavily Doped *P*-Type Si. 2. Optical Modes. *Phys. Rev. B* **1973**, *8*, 4734−4745.
(49) Cerdeira, F.; Cardona, M. Effect of Carrier Concentration on Raman Frequencies of Si and Ge. *Phys. Rev. B* **1972**, *5*, 1440−1454.
(50) Rao, A. M.; Eklund, P. C.; Bandow, S.; Thess, A.; Smalley, R. E. Evidence for Charge Transfer in Doped Carbon Nanotube Bundles from Raman Scattering. *Nature* **1997**, *388*, 257−259.
(51) Mignuzzi, S.; Pollard, A. J.; Bonini, N.; Brennan, B.; Gilmore, I. S.; Pimenta, M. A.; Richards, D.; Roy, D. Effect of Disorder on Raman Scattering of Single-Layer MoS_2. *Phys. Rev. B: Condens. Matter Mater. Phys.* **2015**, *91*, 195411.
(52) Shi, W.; Zhang, X.; Li, X. L.; Qiao, X. F.; Wu, J. B.; Zhang, J.; Tan, P. H. Phonon Confinement Effect in Two-Dimensional Nanocrystallites of Monolayer MoS_2 to Probe Phonon Dispersion Trends Away from Brillouin-Zone Center. *Chin. Phys. Lett.* **2016**, *33*, 057801.
(53) He, Z.; Zhao, R.; Chen, X.; Chen, H.; Zhu, Y.; Su, H.; Huang, S.; Xue, J.; Dai, J.; Cheng, S.; Liu, M.; Wang, X.; Chen, Y. Defect Engineering in Single-Layer MoS_2 Using Heavy Ion Irradiation. *ACS Appl. Mater. Interfaces* **2018**, *10*, 42524−42533.
(54) Chen, Y.; Huang, S. X.; Ji, X.; Adepalli, K.; Yin, K. D.; Ling, X.; Wang, X. W.; Xue, J. M.; Dresselhaus, M.; Kong, J.; Yildiz, B. Tuning Electronic Structure of Single Layer MoS_2 through Defect and Interface Engineering. *ACS Nano* **2018**, *12*, 2569−2579.
(55) Parkin, W. M.; Balan, A.; Liang, L. B.; Das, P. M.; Lamparski, M.; Naylor, C. H.; Rodriguez-Manzo, J. A.; Johnson, A. T. C.; Meunier, V.; Drndic, M. Raman Shifts in Electron-Irradiated Monolayer MoS_2. *ACS Nano* **2016**, *10*, 4134−4142.
(56) Khan, A. I.; Khakbaz, P.; Brenner, K. A.; Smithe, K. K. H.; Mleczko, M. J.; Esseni, D.; Pop, E. Large Temperature Coefficient of Resistance in Atomically Thin Two-Dimensional Semiconductors. *Appl. Phys. Lett.* **2020**, *116*, 203105.
(57) Lee, Y.; Fiore, S.; Luisier, M. *Ab Initio* Mobility of Single-Layer MoS_2 and WS_2: Comparison to Experiments and Impact on the Device Characteristics. *2019 International Electron Devices Meeting (IEDM)* **2019**, 24.24.21−24.24.24.
(58) McCreary, K. M.; Hanbicki, A. T.; Sivaram, S. V.; Jonker, B. T. A- and B-Exciton Photoluminescence Intensity Ratio as a Measure of Sample Quality for Transition Metal Dichalcogenide Monolayers. *APL Mater.* **2018**, *6*, 111106.
(59) Zafar, A.; Nan, H.; Zafar, Z.; Wu, Z.; Jiang, J.; You, Y.; Ni, Z. Probing the Intrinsic Optical Quality of CVD Grown MoS_2. *Nano Res.* **2017**, *10*, 1608−1617.
(60) Mukherjee, B.; Kaushik, N.; Tripathi, R. P.; Joseph, A. M.; Mohapatra, P. K.; Dhar, S.; Singh, B. P.; Kumar, G. V.; Simsek, E.; Lodha, S. Exciton Emission Intensity Modulation of Monolayer MoS_2 *via* Au Plasmon Coupling. *Sci. Rep.* **2017**, *7*, 41175.
(61) Chen, R.; Nuhfer, N. T.; Moussa, L.; Morris, H. R.; Whitmore, P. M. Silver Sulfide Nanoparticle Assembly Obtained by Reacting an Assembled Silver Nanoparticle Template with Hydrogen Sulfide Gas. *Nanotechnology* **2008**, *19*, 455604.
(62) Schroeder, D. K. *Semiconductor Material and Device Characterization*, 3rd ed.; John Wiley & Sons: NJ, 2006.
(63) Saidi, W. A. Trends in the Adsorption and Growth Morphology of Metals on the MoS_2(001) Surface. *Cryst. Growth Des.* **2015**, *15*, 3190−3200.
(64) Arutchelvan, G.; Lockhart de la Rosa, C. J.; Matagne, P.; Sutar, S.; Radu, I.; Huyghebaert, C.; De Gendt, S.; Heyns, M. From the Metal to the Channel: A Study of Carrier Injection through the Metal/2D MoS_2 Interface. *Nanoscale* **2017**, *9*, 10869−10879.
(65) Bampoulis, P.; van Bremen, R.; Yao, Q. R.; Poelsema, B.; Zandvliet, H. J. W.; Sotthewes, K. Defect Dominated Charge Transport and Fermi Level Pinning in MoS_2/Metal Contacts. *ACS Appl. Mater. Interfaces* **2017**, *9*, 19278−19286.
(66) Cheng, Z. H.; Cardenas, J. A.; McGuire, F.; Najmaei, S.; Franklin, A. D. Modifying the Ni-MoS_2 Contact Interface Using a Broad-Beam Ion Source. *IEEE Electron Device Lett.* **2016**, *37*, 1234−1237.
(67) Passi, V.; Gahoi, A.; Marin, E. G.; Cusati, T.; Fortunelli, A.; Iannaccone, G.; Fiori, G.; Lemme, M. C. Ultralow Specific Contact Resistivity in Metal-Graphene Junctions *via* Contact Engineering. *Adv. Mater. Interfaces* **2019**, *6*, 1801285.
(68) Rai, A.; Valsaraj, A.; Movva, H. C. P.; Roy, A.; Ghosh, R.; Sonde, S.; Kang, S. W.; Chang, J. W.; Trivedi, T.; Dey, R.; Guchhait, S.; Larentis, S.; Register, L. F.; Tutuc, E.; Banerjee, S. K. Air Stable Doping and Intrinsic Mobility Enhancement in Monolayer Molybdenum Disulfide by Amorphous Titanium Suboxide Encapsulation. *Nano Lett.* **2015**, *15*, 4329−4336.
(69) Leonhardt, A.; Chiappe, D.; Asselberghs, I.; Huyghebaert, C.; Radu, I.; De Gendt, S. Improving MOCVD MoS_2 Electrical Performance: Impact of Minimized Water and Air Exposure Conditions. *IEEE Electron Device Lett.* **2017**, *38*, 1606−1609.
(70) Liu, W.; Kang, J.; Sarkar, D.; Khatami, Y.; Jena, D.; Banerjee, K. Role of Metal Contacts in Designing High-Performance Monolayer *n*-type WSe_2 Field Effect Transistors. *Nano Lett.* **2013**, *13*, 1983−1990.
(71) Conley, H. J.; Wang, B.; Ziegler, J. I.; Haglund, R. F., Jr.; Pantelides, S. T.; Bolotin, K. I. Bandgap Engineering of Strained Monolayer and Bilayer MoS_2. *Nano Lett.* **2013**, *13*, 3626−3630.
(72) Dai, Z.; Liu, L.; Zhang, Z. Strain Engineering of 2D Materials: Issues and Opportunities at the Interface. *Adv. Mater.* **2019**, *31*, No. e1805417.
(73) Li, H.; Contryman, A. W.; Qian, X. F.; Ardakani, S. M.; Gong, Y. J.; Wang, X. L.; Weisse, J. M.; Lee, C. H.; Zhao, J. H.; Ajayan, P. M.; Li, J.; Manoharan, H. C.; Zheng, X. L. Optoelectronic Crystal of Artificial Atoms in Strain-Textured Molybdenum Disulphide. *Nat. Commun.* **2015**, *6*, 7381.
(74) Zhu, C. R.; Wang, G.; Liu, B. L.; Marie, X.; Qiao, X. F.; Zhang, X.; Wu, X. X.; Fan, H.; Tan, P. H.; Amand, T.; Urbaszek, B. Strain Tuning of Optical Emission Energy and Polarization in Monolayer and Bilayer MoS_2. *Phys. Rev. B: Condens. Matter Mater. Phys.* **2013**, *88*, 121301.
(75) Amani, M.; Chin, M. L.; Mazzoni, A. L.; Burke, R. A.; Najmaei, S.; Ajayan, P. M.; Lou, J.; Dubey, M. Growth-Substrate Induced Performance Degradation in Chemically Synthesized Monolayer MoS_2 Field Effect Transistors. *Appl. Phys. Lett.* **2014**, *104*, 203506.
(76) Ahn, G. H.; Amani, M.; Rasool, H.; Lien, D. H.; Mastandrea, J. P.; Ager, J. W., III; Dubey, M.; Chrzan, D. C.; Minor, A. M.; Javey, A. Strain-Engineered Growth of Two-Dimensional Materials. *Nat. Commun.* **2017**, *8*, 608.
(77) Hosseini, M.; Elahi, M.; Pourfath, M.; Esseni, D. Very Large Strain Gauges Based on Single Layer $MoSe_2$ and WSe_2 for Sensing Applications. *Appl. Phys. Lett.* **2015**, *107*, 253503.
(78) Lee, B.; Park, J.; Han, G. H.; Ee, H. S.; Naylor, C. H.; Liu, W. J.; Johnson, A. T. C.; Agarwal, R. Fano Resonance and Spectrally Modified Photoluminescence Enhancement in Monolayer MoS_2

https://dx.doi.org/10.1021/acsnano.0c03515
ACS Nano 2020, 14, 14798−14808

Integrated with Plasmonic Nanoantenna Array. *Nano Lett.* **2015**, *15*, 3646−3653.
(79) McGilp, J. F. On Predicting the Chemical-Reactivity of Metal-Semiconductor Interfaces. *J. Phys. C: Solid State Phys.* **1984**, *17*, 2249−2254.
(80) Komsa, H. P.; Kotakoski, J.; Kurasch, S.; Lehtinen, O.; Kaiser, U.; Krasheninnikov, A. V. Two-Dimensional Transition Metal Dichalcogenides under Electron Irradiation: Defect Production and Doping. *Phys. Rev. Lett.* **2012**, *109*, 035503.
(81) Saitoh, M.; Nakabayashi, Y.; Uchida, K.; Numata, T. Short-Channel Performance Improvement by Raised Source/Drain Extensions With Thin Spacers in Trigate Silicon Nanowire MOSFETs. *IEEE Electron Device Lett.* **2011**, *32*, 273−275.
(82) Yang, Y. R.; Breil, N.; Yang, C. Y.; Hsieh, J.; Chiang, F.; Colombeau, B.; Guo, B. N.; Shim, K. H.; Variam, N.; Leung, G.; Hebb, J.; Sharma, S.; Ni, C. N.; Ren, J.; Wen, J.; Park, J. H.; Chen, H.; Chen, S.; Hou, M.; Tsai, D.; et al. Ultra Low *p*-Type SiGe Contact Resistance FinFETs with Ti Silicide Liner Using Cryogenic Contact Implantation Amorphization and Solid-Phase Epitaxial Regrowth (SPER). *IEEE Symp. VLSI Technol. Honolulu, HI, Honolulu, HI* **2016**, 74−75.
(83) Schauble, K.; Zakhidov, D.; Yalon, E.; Deshmukh, S.; Grady, R. W.; Cooley, K. A.; McClellan, C. J.; Vaziri, S.; Passarello, D.; Mohney, S. E.; Toney, M. F.; Sood, A. K.; Salleo, A.; Pop, E. Uncovering the Effects of Metal Contacts on Monolayer MoS_2. *arXiv pre-print*, **2020**, https://arxiv.org/abs/2007.14431.

https://dx.doi.org/10.1021/acsnano.0c03515
ACS Nano 2020, 14, 14798−14808

Supporting Information

Uncovering the Effects of Metal Contacts on Monolayer MoS_2

Kirstin Schauble,[1] Dante Zakhidov,[2] Eilam Yalon,[1,3] Sanchit Deshmukh,[1] Ryan W. Grady,[1] Kayla A. Cooley,[4] Connor J. McClellan,[1] Sam Vaziri,[1] Donata Passarello,[5] Suzanne E. Mohney,[4] Michael F. Toney,[5] A. K. Sood,[6] Alberto Salleo,[2] and Eric Pop[1,2,7,*]

[1]Department of Electrical Engineering, Stanford Univ., Stanford, CA 94305, USA. [*]epop@stanford.edu
[2]Department of Materials Science and Engineering, Stanford Univ., Stanford, CA 94305, USA
[3]Present address: Andrew and Erna Viterbi Department of Electrical Engineering, Technion, Haifa, 3200003, Israel
[4]Department of Materials Science and Engineering, The Pennsylvania State Univ., University Park, PA 16802, USA
[5]Stanford Synchrotron Radiation Lightsource, SLAC National Accelerator Laboratory, Menlo Park, CA 94025, USA
[6]Department of Physics, India Institute of Science, Bangalore 560012, India
[7]Precourt Institute for Energy, Stanford Univ., Stanford, CA 94305, USA

1. Raman Analysis Details

For Raman analysis (data shown in main text Figure 1b), we fit the MoS_2 A_1' peaks with a Lorentzian. The MoS_2 E' peaks are fit as follows: for bare MoS_2, a Lorentzian is fit. For monolayer MoS_2 covered by Ti, Sc, and Y, the MoS_2 peaks disappear (Figure S1). For MoS_2 covered by ultrathin Al and Ni, an asymmetric Fano line shape is fit due to observed doping and damage effects (Figure S2). For MoS_2 covered by Au and Ag, two separate Lorentzian peaks are fit because these metals grow in islands on MoS_2 (see Figures S2d and S5), where one peak is from the MoS_2 not contacted by metal, and the other red-shifted peak is from the MoS_2 directly contacted by metal. For these metals, the position and full width at half maximum (FWHM) of the *shifted* peak (MoS_2 contacted by metal) are listed in Table 1 and Figure 4b of the main text.

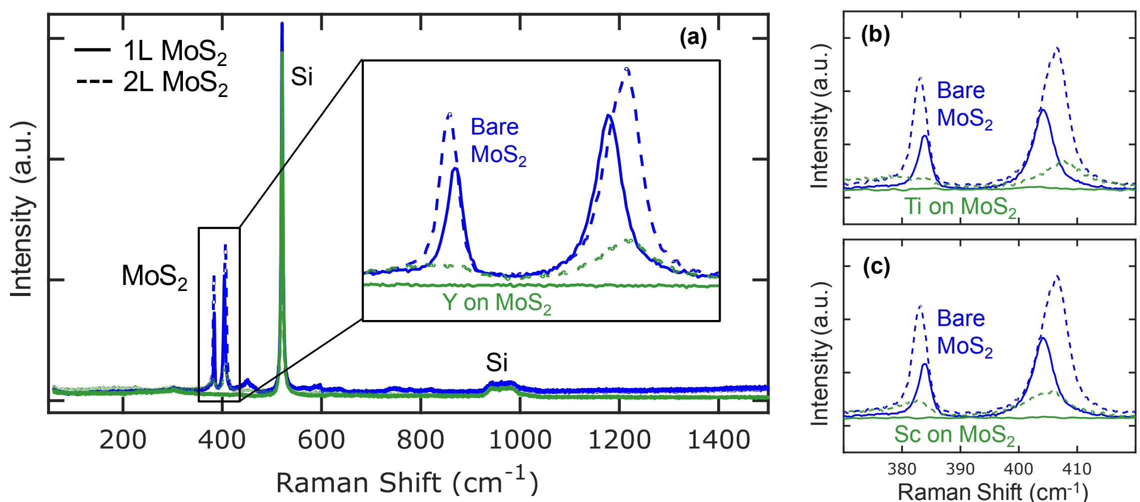

Figure S1: (a) Raman spectra of monolayer (1L, solid lines) and bilayer (2L, dashed lines) MoS_2 bare (blue) and coated with 1.5 nm Y (green), on our SiO_2/Si substrates. The inset shows zoomed in regions of the E' and A_1' MoS_2 peaks (E_g and A_{1g} in bilayer, respectively), where the Raman signal is present for Y on 2L MoS_2 but not 1L, suggesting Y reacts with the top layer but not fully with the bottom layer of 2L MoS_2. Si peaks remain present after Y deposition, which rules out laser reflection from the metal as the cause of the MoS_2 signal disappearance. These data are representative of ~1.5 nm (b) Ti and (c) Sc on MoS_2.

The Fano profile in Figure S2 is defined by $\alpha(\omega) = \alpha_0(q + x)^2/(1 + x^2)$ where α_0 is the prefactor, $x = 2(\omega - \omega_P)/\gamma$, ω is frequency, ω_P is bare phonon frequency, γ is linewidth, and q is the symmetry parameter which depends on electron-phonon coupling strength.[1] A smaller absolute value $|q|$ means more asymmetry and heavier doping. Heavy *n*-type doping shifts the Fermi level near the conduction band, causing interactions between the continuum of electronic states and optical phonons, and thus asymmetry in the Raman peak.

The E' peak of bare MoS_2 has a large $|q|$ showing the most symmetry, as expected. Al-coated MoS_2 has a small $|q|$ and thus large asymmetry, implying heavy doping. In addition, because the mobility under the Al-coated samples remains unchanged but a large negative V_T shift is observed *vs.* the bare samples (see main text Figure 3b), we can ascribe the observed line asymmetry to *n*-type doping and not MoS_2 damage.

Ni-coated MoS_2 has even lower $|q|$ than Al, which would imply heavier MoS_2 doping based on the Fano fit. However, Ni-coated transistors also show the lowest mobility (see main text Figure 4) which suggests MoS_2 sustained the most damage during the evaporation of ultrathin Ni. Because E' peak broadening and asymmetry can be caused by damage (leading to phonon confinement and contribution of dispersive TO modes)[2, 3] we conclude that the asymmetric E' peak of Ni-coated MoS_2 is most likely due to damage.

Finally, the E' Raman peak of Au-coated MoS_2 (Figure S2d) shows a poor Fano fit and is better fit by two separate Lorentzian peaks, as explained above. These two Lorentzians (dashed gray lines) roughly correspond to the LO and TO phonon branches (partly activated by disorder),[2, 3] although a quantitative analysis of their asymmetry and the defect density induced is left to be pursued in future work.

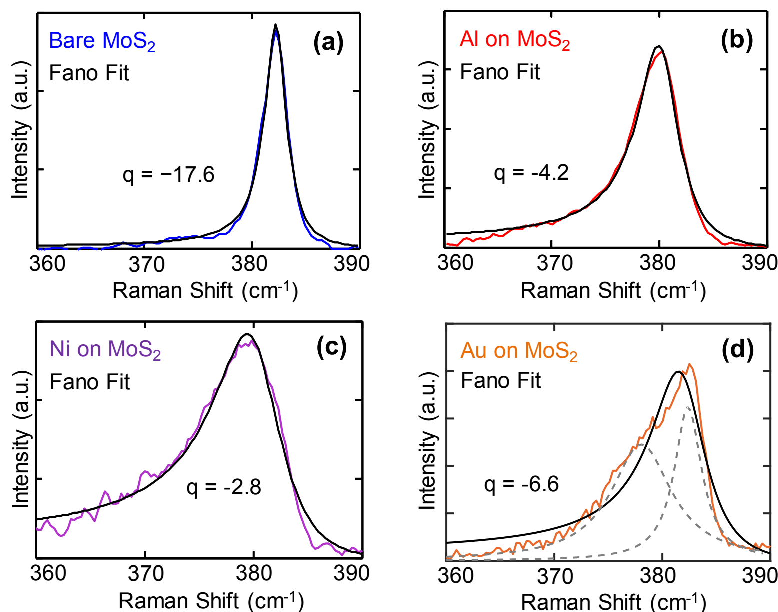

Figure S2: Fano line fits for the E' Raman peak of (a) bare MoS_2, (b) Al, (c) Ni, and (d) Au on MoS_2. The raw data are colored, the Fano fits are solid black lines, the Lorentzian fits in (d) are dashed gray lines.

2. XPS Analysis Details

All XPS spectra are normalized in binding energy (B.E.) by the sp^3 C 1s spectra at 284.8 eV, and normalized in height by the tallest peak in the spectral window. The bare MoS_2 XPS spectra (blue) are shown on the

bottom of Figure S3, and the metal-coated MoS_2 spectra are listed in order of increasing metal work function. The spectra are color-coded based on the observed reactions, described below. We note that the XPS spot size (~100 μm) is much larger than the Raman spot size (<1 μm), so the sparse (~10%) bilayer overgrowth regions of MoS_2 inevitably contribute signal to these data (additional details in Methods), and trace amounts of MoO_x precursor from the growth process may appear in the XPS signal, which will vary depending on the area measured.

First, the bare MoS_2 spectra (plotted in blue) are used as a reference, where the Mo 3d and S 2p spectra are from MoS_2, and the O 1s spectrum shows an SiO_2 substrate peak. Second, Y, Sc, and Ti (plotted in green) react with MoS_2 and oxidize. For MoS_2 coated with these metals, a shift in the Mo 3d spectrum is seen, indicating sulfur-deficient MoS_{2-x} and metallic Mo are left behind after the metals react with the sulfur from MoS_2 (detailed peak fitting of Ti on MoS_2 is provided in Figure 2 of the main text). These metals also induce broadening of the MoS_2 S 2p spectra, indicating metal-sulfide bonding. Note that the Y-coated MoS_2 S 2p spectrum is washed out by a large Y peak (Fig. S3d); however, the shifting of the S 2s signal on the low binding energy side of the Mo 3d spectrum supports the conclusion that Y reacts with the sulfur in MoS_2. We also see a shift in the O 1s spectra, which indicates signal from Ti, Sc, and Y oxides instead of the SiO_2 substrate. Third, Al and Ni (plotted in purple) oxidize but do not react with MoS_2. The Mo 3d and S 2p spectra remain relatively unchanged, indicating that MoS_2 is still present and no reactions with the metal take place. Note that the Ni-covered MoS_2 sample shows an increase in MoO_x signal (at B.E. ≈ 236 eV), which is likely caused by the degradation of MoS_2 due to Ni deposition, as evidenced by broadening of the Raman peaks (main text Fig. 1b) and decreased electrical mobility (main text Fig. 4). The O 1s spectra are shifted, indicating that the signal is from Al and Ni oxides instead of the SiO_2 substrate. Lastly, Ag and Au (plotted in black) do not react with MoS_2 or oxidize. The Mo 3d, S 2p, and O 1s spectra remain relatively unchanged from the bare MoS_2 spectrum. The S 2p spectrum of Ag-capped MoS_2 shows broadening, suggesting sulfurization of Ag. However, since the MoS_2 Mo 3d peaks unaffected, and cross-section TEM images (Fig. 4d in main text) reveal a pristine interface, we conclude that the sulfurization of Ag is due to Ag tarnishing from sulfur-containing gases in ambient air instead of reactions with MoS2.

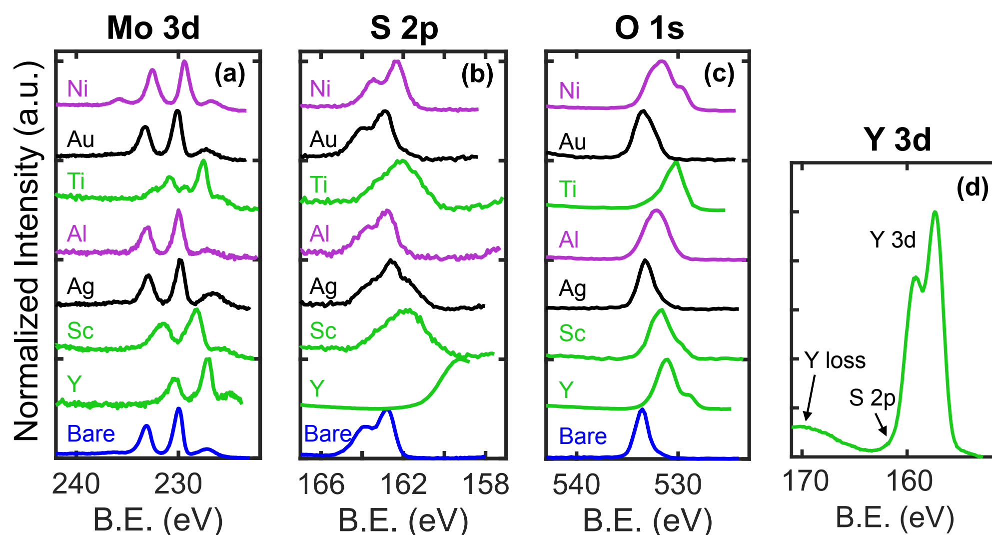

Figure S3: (a) XPS Mo 3d spectra shows doublet Mo 3d5/2 and Mo 3d3/2 peaks. (b) XPS S 2p spectra shows doublet S 2p3/2 and S 2p1/2 peaks. (c) XPS O 1s spectra shows SiO_2 or oxidized metals. (d) XPS Y 3d spectrum shows overlap between large Y3d peak and weak S 2p peak.

3. SAED and TEM Data

Figure S4 shows selected area electron diffraction (SAED) patterns for MoS_2 coated with ultrathin Ag and Ni on TEM grids (see Methods for sample preparation). For Ag-coated MoS_2, in addition to polycrystalline MoS_2 and Ag, an additional crystalline phase is present and can be attributed to Ag_2S or Mo_8O_{23}. For the Ni-coated sample, there is no evidence of crystalline phases besides MoS_2, indicating that Ni is oxidizing into an amorphous phase. These results are consistent with XPS data in Figure S3.

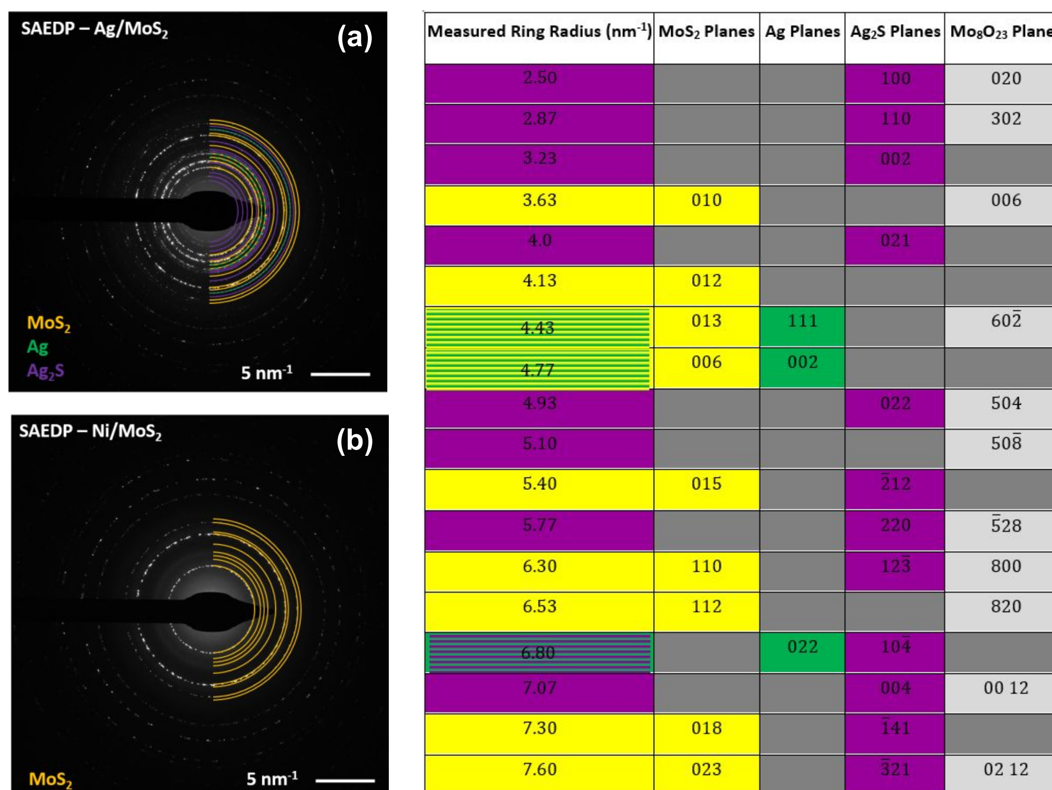

Measured Ring Radius (nm^{-1})	MoS_2 Planes	Ag Planes	Ag_2S Planes	Mo_8O_{23} Planes
2.50			100	020
2.87			110	302
3.23			002	
3.63	010			006
4.0			021	
4.13	012			
4.43	013	111		$60\bar{2}$
4.77	006	002		
4.93			022	504
5.10				$50\bar{8}$
5.40	015		$\bar{2}12$	
5.77			220	$\bar{5}28$
6.30	110		$12\bar{3}$	800
6.53	112			820
6.80		022	$10\bar{4}$	
7.07			004	00 12
7.30	018		$\bar{1}41$	
7.60	023		$\bar{3}21$	02 12

Figure S4: SAED pattern of (a) Ag-coated MoS_2 and (b) Ni-coated MoS_2. The table identifies SAED diffraction planes for each ring in the Ag/MoS_2 system. The interplanar spacing (not shown) for the given phases was determined from crystal structures on the Crystallography Open Database.[4] Ring radii are colored according to the SAED diffraction plane identification (using the calculated interplanar spacing values): MoS_2 (yellow), Ag (green), Ag_2S (purple), and Mo_8O_{23} (gray). Rows with two striped colors indicate that diffraction planes exist with the given ring radius for both materials.

Figure S5 shows additional plan view TEMs, revealing Au and Ag non-uniformly "ball up" when deposited on MoS_2 into ~10 to 20 nm size islands. Au (also in main text Figure 4c) shows slightly denser nucleation on SiO_2 than MoS_2, whereas it is difficult to see contrast of MoS_2 edges at this scale on the Ag sample due to high contrast between MoS_2 and Ag. Al and Ni also deposit as discontinuous films on MoS_2, where Ni was found to completely oxidize but some unoxidized Al signal was present in EDS. Ag and Au did not oxidize, consistent with XPS (Figure S3). Al on MoS_2 (also in main text Figure 3c) has the largest island size, as well as increased continuity on MoS_2 than SiO_2. Ni islands are very small (~2-3 nm), but upon careful examination we find that they are discontinuous and nucleate with similar density on MoS_2 and SiO_2. These results are consistent with predictions of Au, Ag, and Ni island growth morphology on MoS_2 based on the adhesion energies and diffusion barriers of metal monomers on MoS_2, where Ni was also predicted to form much smaller islands due to its larger diffusion barrier.[5]

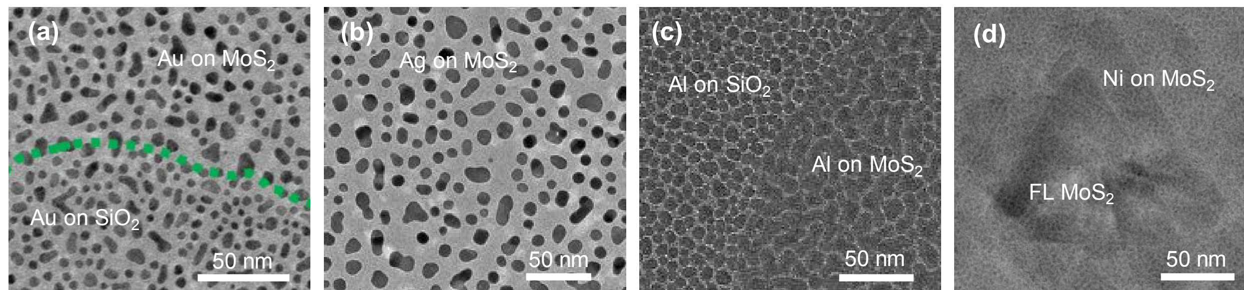

Figure S5: Plan view TEM of ultrathin (a) Au, (b) Ag, (c) Al, and (d) Ni on as-grown monolayer MoS_2.

4. Enthalpy of Formation Analysis

Table S1 displays enthalpy of formation of MoS_2, metal oxides, and metal sulfides, in kJ per mole of solid S for the sulfides and gaseous O_2 for the oxides (their most stable forms). Y, Sc, and Ti sulfides have enthalpies of formation that are more negative than MoS_2, meaning the sulfur atoms in MoS_2 prefer to bond with Y, Sc, and Ti rather than Mo, assuming small entropies of formation and no kinetic limitations. Ag, Au, and Ni have less negative enthalpies of formation with sulfur (or nonexistent in the case of Au), and thus their reactions with MoS_2 are thermodynamically unlikely (consistent with our XPS data).

Al is thermodynamically expected to react with MoS_2, but none of our results indicate a reaction between Al and MoS_2. This has also been observed in previous studies,[6, 7] and can be explained by a larger kinetic barrier for reaction with sulfur, or by Al oxidation since Al_2O_3 has a much more negative enthalpy of formation (Table S1). In addition, Al has the lowest melting temperature and requires the lowest power evaporation of all metals studied, so its deposition may induce fewer MoS_2 defects than other metals during evaporation, which could prevent a reaction with MoS_2 (assuming that defects mediate the reaction).

We note that full thermodynamic analysis would involve the Gibbs free energy, which includes the entropy of formation, and the construction of a phase diagram.[8] However, many entropy values required for such an analysis are either unavailable or have large error bars, so we use enthalpy of formation for rapid but approximate insight. To make a fairer comparison, we report values per mole of solid S (sulfides) or gaseous O_2 (oxides), allowing the larger entropy term for gaseous O_2 to cancel in the comparison among oxides.

	Enthalpy of Formation (kJ/mol)					
	S	Result	Ref.	O	Result	Ref.
Mo	**-138**	**MoS_2**	9	-548	MoO_2	10
Ni	-74	NiS_2	9	**-485**	**NiO**	10
Au		--			--	
Ti	**-205**	**TiS_2**	11	**-1046**	**$Ti_{1.43}O$**	10
Al	-151	AlS	9	**-1116**	**Al_2O_3**	10
Ag	**-32**	**Ag_2S**	12	-61	Ag_2O	10
Sc	**-774**	**$Sc_{0.8065}S$**	13	**-1088**	**Sc_2O_3**	10
Y	**-262**	**YS**	14	**-1121**	**Y_2O_3**	10

Table S1: Thermodynamic enthalpy of formation for sulfides and oxides of the metals studied at room temperature. Bolded values are the reactions seen experimentally in XPS data (from Figure S3).

5. Additional Electrical Measurements

Figure S6 shows an example pseudo-TLM mobility extraction (following Smithe *et al.*[15]) for a bare MoS_2 channel, where the same analysis is done to calculate the mobility of the MoS_2 channel after depositing each non-reacting metal. The resulting mobility values for MoS_2 devices bare and coated with each non-reacting metal are reported in the main text Figure 4b, and are found to degrade drastically after deposition of Ni, Au, and Ag. Note that while the channel lengths here are too long to accurately extract contact resistance, mobility values can be estimated from the sheet resistance (slope of R_{TOT} *vs.* L).

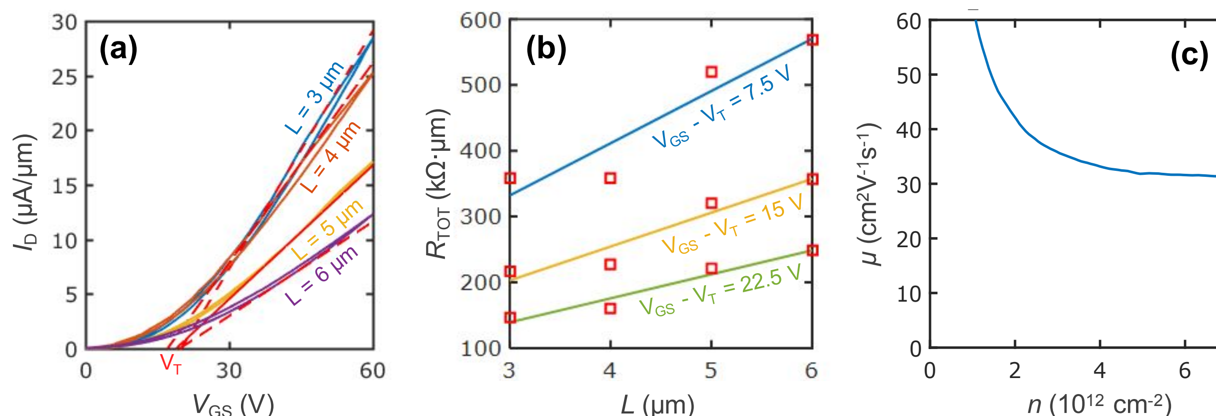

Figure S6: Example of pseudo-transfer length method (TLM)[15] extraction of mobility for bare (uncapped) monolayer MoS_2 devices. (a) Measured drain current *vs.* back-gate voltage (I_D *vs.* V_{GS}) at V_{DS} = 1 V for channel lengths 3 to 6 μm. Red dashed lines show linear extrapolation[15] to find threshold voltage V_T. (b) Total device resistance R_{TOT} *vs.* channel length (L) measured by TLM at various gate overdrives (V_{GS} - V_T). (c) Estimated effective mobility (μ) *vs.* carrier density (n) based on $\mu = (qnR_{SH})^{-1}$, where sheet resistance R_{SH} is the slope of R_{TOT} *vs.* L in (b). Figure 4c in the main text displays this mobility (for bare, Ag-, Au-, and Ni-coated samples) at $n \approx 7 \times 10^{12}$ cm^{-2}.

Figure S7 shows electrical measurements of MoS_2 capped with ultrathin Ti, Sc, and Y. These data are representative of several devices measured. Ti- and Y-coated MoS_2 devices lost nearly all gate dependence, and any conduction is due to byproducts of the reaction between the metal and MoS_2 (see Raman data in Figure S1 and XPS data in Figure S3). Sc-coated MoS_2 devices still show gate dependence, indicating some semiconducting behavior in the device channel, which must be due to either remaining MoS_2 (*e.g.* under bilayer regions) or byproducts of the Sc reaction with MoS_2 (ScS is an *n*-type conductor).[16] Additionally, we note the device channels had gone through several rounds of photolithography prior to ultrathin metal evaporation, so any residual photoresist may hinder interfacial reactions.

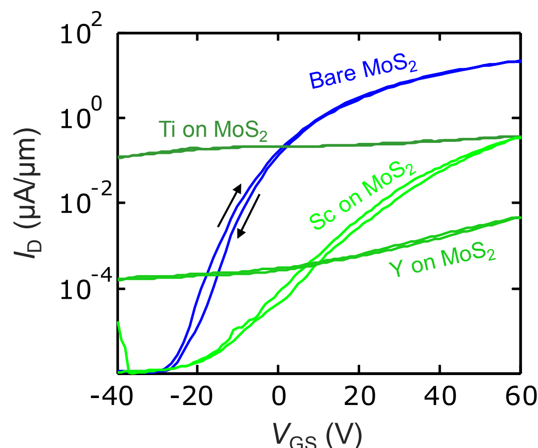

Figure S7: Measured drain current *vs.* back-gate voltage (I_D *vs.* V_{GS}) of monolayer MoS_2 devices coated with ultrathin films (~1.5 nm) of low work function metals (Y, Sc, and Ti). $L = 3$ µm, $V_{DS} = 1$ V. Small arrows show the sweep direction, revealing repeatable measurements with minimal hysteresis. These data are representative of 5-10 devices measured for each kind of ultrathin metal coverage.

6. XRD Analysis Details

In order to calculate the built-in strain of our monolayer MoS_2 grown by chemical vapor deposition (CVD), we transfer (with the process described by Vaziri *et al.*[17]) the as-grown MoS_2 onto a fresh SiO_2/Si substrate and measure the strain before and after transferring (without any contact metals). This analysis assumes that transferring the MoS_2 releases its built-in strain. Figure S8 displays Raman and X-ray diffraction (XRD) data of as-grown and transferred MoS_2. Using Raman-based strain analysis, we find that the as-grown MoS_2 is tensile strained ~0.4 to 0.5%, based on a calibration of 4.5 cm^{-1} E' peak shift per % biaxial strain as reported by Li *et al.*[18] XRD-based strain analysis uses Bragg's law to calculate the spacing between (10) rows of MoS_2 atoms in the 2D layer, $d = n\lambda/[2\sin(\theta)]$, where the X-ray wavelength $\lambda = 0.886$ Å (14 keV) and n is the order of reflection [here $n = 1$ for the MoS_2 (10) rows, $n = 2$ for MoS_2 (20) rows, etc.]. XRD analysis verifies that the Raman-based estimates of built-in MoS_2 tensile strain after CVD growth are accurate, as seen in Figure S8c. Raman and XRD analysis are in agreement for measuring built-in strain of bare MoS_2, however we show in the main text Figure 5 that Raman analysis is not predictive in determining strain of MoS_2 under contact metals, ostensibly due to the metal influence on the E' peak shift.

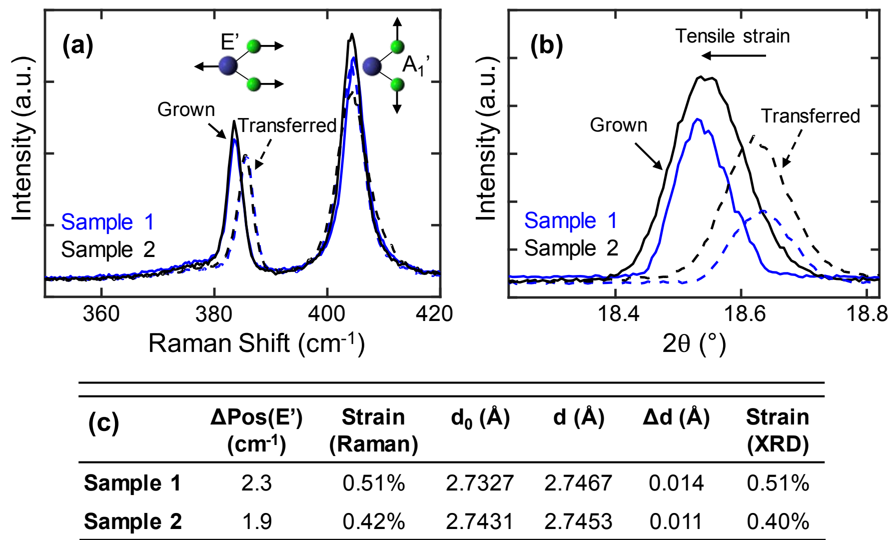

(c)	ΔPos(E') (cm^{-1})	Strain (Raman)	d_0 (Å)	d (Å)	Δd (Å)	Strain (XRD)
Sample 1	2.3	0.51%	2.7327	2.7467	0.014	0.51%
Sample 2	1.9	0.42%	2.7431	2.7453	0.011	0.40%

Figure S8: (a) Raman spectra of transferred *vs.* as-grown MoS_2, reveal E' peak red shifts corresponding to ~0.4 to 0.5% tensile strain, depending on the particular growth. (b) Grazing incidence XRD of transferred *vs.* as-grown monolayer MoS_2 in-plane (10) peak. The XRD peak shift also reveals ~0.4 to 0.5% biaxial tensile strain in the as-grown MoS_2. Note Raman data are point spectra over < 1 μm^2 regions (the laser spot size) whereas XRD averages over an effective measurement area of 2.8 mm by the whole length of the sample (7-12 mm). (c) Table shows Raman-based MoS_2 strain calculated from change in E' peak position after transfer, and XRD-based MoS_2 strain calculated from change in *d* spacing after transfer ($\Delta d/d_0$). d_0 is *d*-spacing after transfer (assumed unstrained), *d* is before transfer (tensile strained), and Δd is the change.

Figure S9 displays Williamson-Hall XRD analysis of bare CVD-grown MoS_2, a method where peak broadening due to crystallite size and microstrain is deconvoluted by considering the peak width (FWHM of "as-grown" MoS_2 peaks in Figure S8b) as a function of X-ray Bragg angle θ. The Williamson-Hall formula (inset in Figure S9) shows a linear relationship between the (10), (20), and (30) peak FWHM (= B_{sample}) multiplied by cos(θ) as a function of sin(θ).[19] The y-intercept of this model gives information on the crystallite size, where K is the Scherrer coefficient, and the slope gives the microstrain within the crystallites, as fit with dashed lines in Figure S9. We find that with K = 1.05,[20] the average crystallite size is 61 ± 4.2 nm, which is smaller than the grain size of the MoS_2 film, as the estimated crystallite size is affected by line defects, dislocations, stacking faults, or other disorder. We also estimate the average microstrain in all four samples is 0.084 ± 0.047%, *i.e.* the distribution of strains across the crystallites.

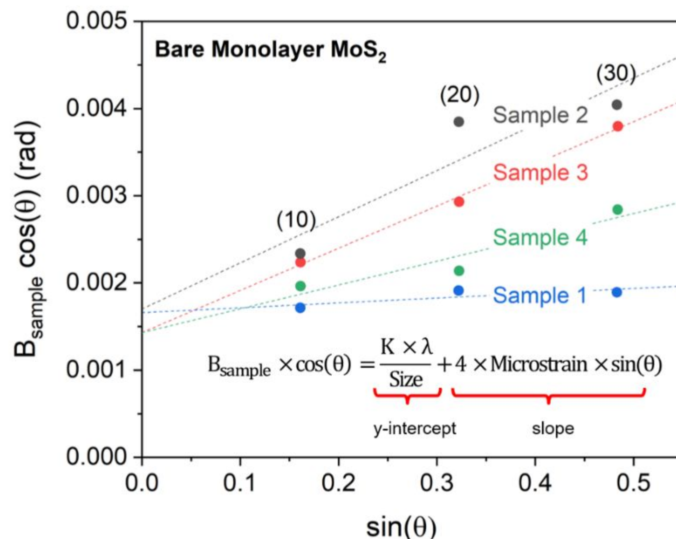

Figure S9: Williamson-Hall analysis of four different bare, as-grown monolayer MoS_2 growths (on our typical SiO_2/Si substrates) using grazing incidence XRD data, where each color represents a different growth. The dashed lines represent linear fits to the scattered data points.

Figure S10 shows the spacing d between (10) rows of MoS_2 atoms measured by grazing incidence XRD (calculated from XRD 2θ scans, in main text Figure 5a). Average strain is calculated based on change in lattice spacing relative to the as-grown monolayer MoS_2 ($\Delta d/d$), indicating no change in MoS_2 strain due to ultrathin metal capping. We note that in the case of contact metals on MoS_2, it was not possible to do a Williamson-Hall analysis due to poor signal-to-noise ratio of the (20) peak. As a result, the FWHMs reported in Figure S10 embody the microstrain in addition to other broadening effects such as crystallite size. Overall, the FWHM of the MoS_2 (10) XRD peak is similar between bare MoS_2 and MoS_2 capped with ultrathin metals, indicating no significant changes in MoS_2 strain distribution or crystallite size due to metals. However, from transport measurements (main text Figure 4b) we note that some metals, especially Ni, introduce point defects which reduce the electron mobility. (XRD is not sensitive to these point defects.)

	d spacing (Å)	Strain based on d-spacing	FWHM (°)
Bare MoS_2	2.7429	--	0.12
Ag on MoS_2	2.7430	0.003%	0.12
Au on MoS_2	2.7432	0.012%	0.13
Al on MoS_2	2.7433	0.014%	0.12
Ni on MoS_2	2.7439	0.037%	0.11

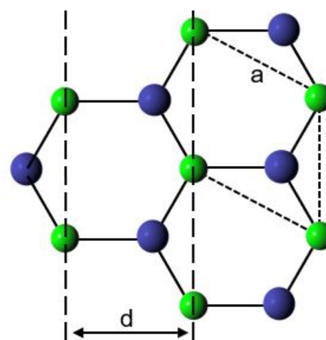

Figure S10: Table shows measured d-spacing between (10) rows of atoms, calculated strain, and MoS_2 (10) XRD peak FWHM values for bare as-grown MoS_2 and coated with each non-reacting metal. The strain listed is *relative* to the as-grown bare MoS_2 in the top row (itself ~0.4 to 0.5% tensile strained with respect to transferred MoS_2, see Figure S8). Figure (right) shows the physical distance $d = 3^{1/2}a/2$ measured by XRD, where a = 3.167 Å (for our tensile strained as-grown MoS_2). We note a_0 = 3.15 Å is the accepted (unstrained) lattice constant of bulk MoS_2.[21, 22]

For XRD measurements, the sample was attached to a six-circle diffractometer and rotated vertically in the χ direction (Figure S11). The sample was covered with a Kapton dome (not shown) and purged with helium gas to improve the signal-to-noise ratio by reducing air scattering and to reduce sample damage. The 14 keV (0.886 Å) incident beam was set to grazing incidence (ω = 0.1°) and the scattered radiation was collimated to 1 mrad by Soller slits and collected by a Vortex point detector. The sample was rocked up and down in the z direction during the measurement to reduce potential beam damage, and each measurement was averaged over 3 exposures to reduce noise.

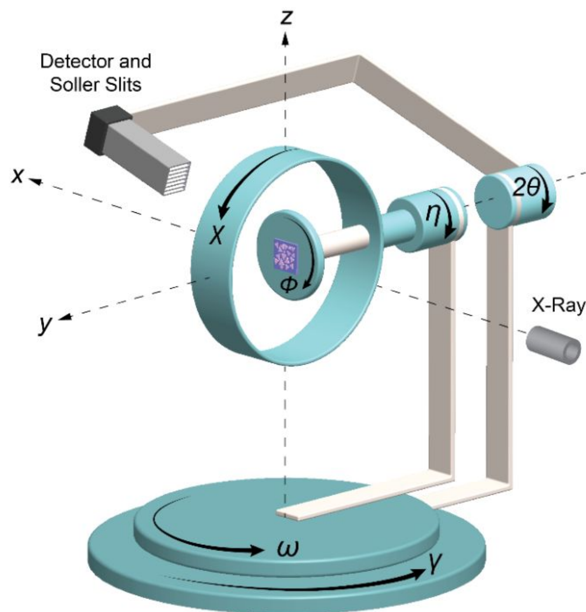

Figure S11: X-ray diffraction geometry at the Stanford Synchrotron Radiation Lightsource. The purple square represents the sample, with the small triangles symbolizing polycrystalline MoS_2 grains. The labels x, y, and z define the 3D coordinate system, and labels η, ϕ, χ, γ, ω, and 2θ define rotational degrees of freedom. 2θ sweeps the detector arm during measurement and ω sets the incidence angle. Note that η, ϕ, χ, and γ are not used during measurement and, in this configuration, η serves the same purpose as ϕ.

7. Supplementary References

1. Nickel, N. H.; Lengsfeld, P.; Sieber, I., Raman Spectroscopy of Heavily Doped Polycrystalline Silicon Thin Films. *Phys. Rev. B* **2000,** *61*, 15558-15561.
2. Mignuzzi, S.; Pollard, A. J.; Bonini, N.; Brennan, B.; Gilmore, I. S.; Pimenta, M. A.; Richards, D.; Roy, D., Effect of Disorder on Raman Scattering of Single-Layer MoS_2. *Phys. Rev. B* **2015,** *91*, 195411.
3. Shi, W.; Zhang, X.; Li, X. L.; Qiao, X. F.; Wu, J. B.; Zhang, J.; Tan, P. H., Phonon Confinement Effect in Two-Dimensional Nanocrystallites of Monolayer MoS_2 to Probe Phonon Dispersion Trends Away from Brillouin-Zone Center. *Chinese Phys. Lett.* **2016,** *33*, 057801.
4. Crystallography Open Database. http://www.crystallography.net/cod/ (accessed February 10, 2019).
5. Saidi, W. A., Trends in the Adsorption and Growth Morphology of Metals on the MoS_2(001) Surface. *Cryst. Growth Des.* **2015,** *15*, 3190-3200.
6. Lince, J. R.; Carre, D. J.; Fleischauer, P. D., Schottky-Barrier Formation on a Covalent Semiconductor without Fermi-Level Pinning: The Metal-MoS_2(0001) Interface. *Phys. Rev. B* **1987,** *36*, 1647-1656.
7. McGovern, I. T.; Dietz, E.; Rotermund, H. H.; Bradshaw, A. M.; Braun, W.; Radlik, W.; Mcgilp, J. F., Soft-X-Ray Photoemission Spectroscopy of Metal Molybdenum-Disulfide Interfaces. *Surf. Sci.* **1985,** *152*, 1203-1212.

8. Domask, A. C.; Gurunathan, R. L.; Mohney, S. E., Transition Metal-MoS_2 Reactions: Review and Thermodynamic Predictions. *J. Electron. Mater.* **2015,** *44*, 4065-4079.
9. Chase, M. W., *NIST-JANAF Thermochemical Tables*; 4th Edition. American Institute of Physics: **1998**.
10. Brewer, L., The Thermodynamic Properties of the Oxides and Their Vaporization Processes. *Chem. Rev.* **1952,** *51*, 1.
11. O'Hare, P. A. G.; Johnson, G. K., Thermochemistry of Inorganic Sulfur Compounds VII. Standard Molar Enthalpy of Formation at 298.15 K, High-Temperature Enthalpy Increments, and Other Thermodynamic Properties to 1100 K of Titanium Disulfide, TiS_2. *J. Chem. Thermodyn.* **1986,** *18*, 189.
12. Thompson, W. T.; Flengas, S. N., Drop Calorimetric Measurements on Some Chlorides, Sulfides, and Binary Melts. *Can. J. Chem.* **1971,** *49*, 1550.
13. Nakahara, J. F. The Electronic Structure and Thermodynamics of Scandium Monosulfide. Iowa State University, Retrospective Theses and Dissertations, 1984.
14. Gschneider, K. A. J.; Kippenhan, N. *Thermochemistry of the Rare Earth Carbides, Nitrides, and Sulfides for Steelmaking*; IS-RIC--5; Iowa State Univ. of Science and Technology, Ames (USA): Rare-Earth Information Center, 1971; p 20.
15. Smithe, K. K. H.; Suryavanshi, S. V.; Muñoz Rojo, M.; Tedjarati, A. D.; Pop, E., Low Variability in Synthetic Monolayer MoS_2 Devices. *ACS Nano* **2017,** *11*, 8456-8463.
16. Dismukes, J. P.; White, J. G., The Preparation, Properties, and Crystal Structures of Some Scandium Sulfides in the Range Sc_2S_3-ScS. *Inorganic Chemistry* **1964,** *3*, 1220-1228.
17. Vaziri, S.; Yalon, E.; Munoz Rojo, M.; Suryavanshi, S. V.; Zhang, H.; McClellan, C. J.; Bailey, C. S.; Smithe, K. K. H.; Gabourie, A. J.; Chen, V.; Deshmukh, S.; Bendersky, L.; Davydov, A. V.; Pop, E., Ultrahigh Thermal Isolation Across Heterogeneously Layered Two-Dimensional Materials. *Science Advances* **2019,** *5*, eaax1325.
18. Li, H.; Contryman, A. W.; Qian, X. F.; Ardakani, S. M.; Gong, Y. J.; Wang, X. L.; Weisse, J. M.; Lee, C. H.; Zhao, J. H.; Ajayan, P. M.; Li, J.; Manoharan, H. C.; Zheng, X. L., Optoelectronic Crystal of Artificial Atoms in Strain-Textured Molybdenum Disulphide. *Nat. Commun.* **2015,** *6*, 7381.
19. Warren, B. E., *X-Ray Diffraction*; Dover Publications: New York, **1990**.
20. Lele, S.; Anantharaman, T. R., Influence of Crystallite Shape on Particle Size Broadening of Debye-Scherrer Reflections. *Proc. Indian Acad. Sci.* **1966,** *64*, 261-274.
21. Dickinson, R. G.; Pauling, L., The Crystal Structure of Molybdenite. *J. Am. Chem. Soc.* **1923,** *45*, 1466-1471.
22. Wakabayashi, N.; Smith, H. G.; Nicklow, R. M., Lattice Dynamics of Hexagonal MoS_2 Studied by Neutron Scattering. *Phys. Rev. B* **1975,** *12*, 659-663.